Department of Electrical and Information Engineering
ELECTRICAL AND INFORMATION ENGINEERING
Ph.D. Program
SSD: ING-IND/31–ELECTRICAL ENGINEERING

Final Dissertation

Micromagnetic modeling for the design of spintronic sensors and logic gates devices

---

by
Francesco Cutugno

Supervisor:

Prof. Mario Carpentieri

Coordinator of Ph.D. Program:
Prof. Mario Carpentieri

Course n°35, 01/11/2019-31/01/2023

Politecnico di Bari

Department of Electrical and Information Engineering
ELECTRICAL AND INFORMATION ENGINEERING
Ph.D. Program
SSD: ING-IND/31–ELECTRICAL ENGINEERING

Final Dissertation

Micromagnetic modeling for the design of spintronic sensors and logic gates devices

---

by
Francesco Cutugno:

_____

Referees:

Prof. Óscar Alejos Ducal

Prof. Luis Torres Rincón

Supervisor:

Prof. Mario Carpentieri

Coordinator of Ph.D Program:
Prof. Mario Carpentieri
firma

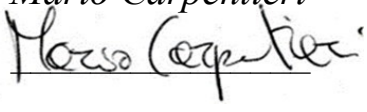

Course n°35, 01/11/2019-31/01/2023

Acknowledgements

It is certainly not an easy task to be able to thank, in a few lines and with a personal touch, all those who, in one way or another, have helped me during these three years of my doctorate.

First of all, I want to thank my supervisor, Professor Mario Carpentieri. Thank you for your patience and availability you had during this journey, as well as, I want to thank you for sharing your knowledge with me. So, thank you for your guidance and for your time.

Secondly, I thank all the members of the Petaspin group, present and past, Vito, Riccardo, Anna, Andrea, Eleonora, Pietro, Luciano, Celeste, Andrea and all the others, with particular attention to Professor Giovanni Finocchio. Thank you all, it has been a privilege, an honor and a pleasure to have been able to grow and collaborate with you. Thank you.

After that, I want to thank the guys from the University of Valladolid, where I spent my period abroad. Óscar, Luis and the others from the electronics and electromagnetism group, thank you for the great experience.

I want to thank Professor Marco Lanuzza and his collaborators, Esteban and Raffaele, with whom I had the opportunity to collaborate. Thank you.

As a special mention, I want to extend my gratitude to professors Giovanni Carlotti and Ermanno Cardelli, thanks to whom I have found the passion and desire to embark on this journey. Thanks for everything.

Thanks to my family, because they supported me before and during this fantastic journey that I decided to undertake with difficulty. Thank you for the tenacity and perseverance you have taught me, absolutely necessary to

be able to resist in this world. Thank you.

I thank my friends, the old ones and the new ones I've found along this journey, for supporting and bearing with me over the years. Thank you for the company and for all the moments of fun and growth.
In particular, I want to thank all those who have been my roommates up to this point. Thank you for bearing with me as I wandered around at night looking for the will and energy to keep working.

Last, but not least, I want to thank my girlfriend. Thank you for taking care of me and being by my side, especially in the grayest moments, because it was precisely in those moments that I needed it. Thank you with all my heart.

Abstract

Micromagnetic modeling is a powerful approach that allows to study, design and optimize spintronic devices in an affordable, reliable and relatively quick way.

For the next generation nanoelectronics, among the most promising devices are the spintronic ones. The spin-based technologies result particularly interesting due to their properties: nanometer size, low energy consumption, non-volatility, high scalability, large speed and CMOS integrability. Moreover, spintronic devices are incredibly versatile in terms of applications.

One of the most important spintronic structures is the magnetic tunnel junction (MTJ), that can be schematized as a sandwich of two magnetic layers intercalated by an oxide barrier. MTJs, depending on the input, show a plethora of possible applications, such as memories, amplifiers, nano-oscillators, sensors or diodes. Moreover, the application possibilities of spintronic devices can be further extended. In fact, by designing them with different materials, exploiting the different properties, for example, of ferromagnets or ferrimagnets, their applications can range from megahertz to terahertz.

Three applications are presented in this thesis: first, it is shown how to perform in-memory logic operations with a MTJ as a logic unit, without any intermediate electronic circuitry. Here, the operations are performed without any applied external magnetic field, by exploiting the Voltage Controlled Magnetic Anisotropy (VCMA). The basic structure consists of two MOSFET access devices and two MTJs, in a specular configuration,

connected in series. The IMP and NOT logic operations are chosen as logic bases for operations and are performed only by supplying a DC voltage to the circuit structure.

Second, it is studied the effect of an external magnetic field applied to a nonresonant low-frequency-tail spin-torque diode at room temperature. The system is analyzed in terms of DC output voltage. The existence of a range of values of the injected AC current that promotes a linear behavior of the output voltage of field down to the pT range is shown, that is useful for the development of a magnetic field sensor.

Finally, a transition metal/rare earth ferrimagnet (FiM) system in a spin Hall geometry is analyzed micromagnetically. In particular, the current-driving magnetization dynamics of the system is studied as a function of the uncompensation parameter of the angular momentum of the two sublattices. The interest in FiM materials for spin-based devices are their combination of the ultrafast dynamics, typical of antiferromagnets, with an easier way to control the magnetic state, which is typical of ferromagnets. Other than the possible dynamics, two particular interesting effects are shown: the first is that a self-oscillation is the only possible dynamical state at the angular momentum compensation point, while the second is a finite discontinuity near the magnetization compensation point originated by the demagnetizing field which controls the type of dynamics behind the switching. It is finally shown how interfacial Dzyaloshinskii-Moriya interaction (DMI) affects frequency and amplitude on switching time and self-oscillations of the magnetization.

Table of Contents

List of figures

List of Tables

List of Acronyms

GMR	Giant Magnetoresistance
MTJ	Magnetic Tunnel Junction
FL	Free Layer
PL	Pinned Layer
TMR	Tunnel Magnetic Resistance
FD	Finite Difference
LLG	Landau-Lifshitz-Gilbert
DMI	Dzyalonshinskii-Moriya Interaction
IDMI	Interfacial Dzyalonshinskii-Moriya interaction
VCMA	Voltage Controlled Magnetic Anisotropy
LLGS	Landau–Lifshitz–Gilbert–Slonczewski
SOT	Spin Orbit Torque
FM	Ferromagnet
FiM	Ferrimagnet
AFM	Antiferromagnet
HM	Heavy Metal
STD	Spin-Torque Diode
DC	Direct Current
AC	Alternate Current
IMP	Implication
STD	Spin-Torque Diode
AMCP	Angular Momentum Compensation Point
MCP	Magnetization Compensation Point

Introduction

Electronics, starting from the last past century until nowadays, has one of the most remarkable technological impact, not only in the research or military field, but also in our everyday life. The principle of electronics is to exploit the electronic charge as information carrier that is wanted to be processed, transmitted or detected. From quantum mechanics, it is known that the electron has another degree of freedom, and this can be used with the same purpose: the spin angular momentum.

In the second part of the 80s, based on the groundbreaking works on ferromagnetism/superconducting tunneling experiments [1] and the initial experiments by Jullière on magnetic tunnel junctions [2], with the observation of the injection of spin-polarized electrons from a ferromagnetic metal to a normal metal by Johnson and Silsbee (1985) [3] and the discovery of giant magneto-resistance (GMR) by Albert Fert et al. [4] and Peter Grünberg et al. (1988) [5], the spin electronics was born.

This research field, better known as Spintronics, is considered one of the branches of research most promising for the improvement of the semiconductors-based electronics.

Micromagnetics is one of the most powerful tool that has helped in developing the spin-based electronics, supporting the study of magnetism and magnetic materials. Its origin could be set in 1935 with the study of magnetic domain walls by Landau and Lifshitz [6], obtaining the required attention in 1957 [7], when rigorous nucleation field theory was formulated [8]. Micromagnetics has a key role both based on its theoretical importance and on its technological relevance, helping to design and

optimize spintronic devices, as well as by supporting the experimental works, providing insightful answers about its behavior [9]–[11].

One of the most common spintronic devices is the Magnetic Tunnel Junction (MTJ), which is a multilayer device consisting of two ferromagnetic (FM) layers, one free of modifying its magnetization, called free layer (FL) and one with magnetization fixed, called pinned layer (PL) usually separated by a tunnel oxide barrier, often MgO (Figure 0.1).

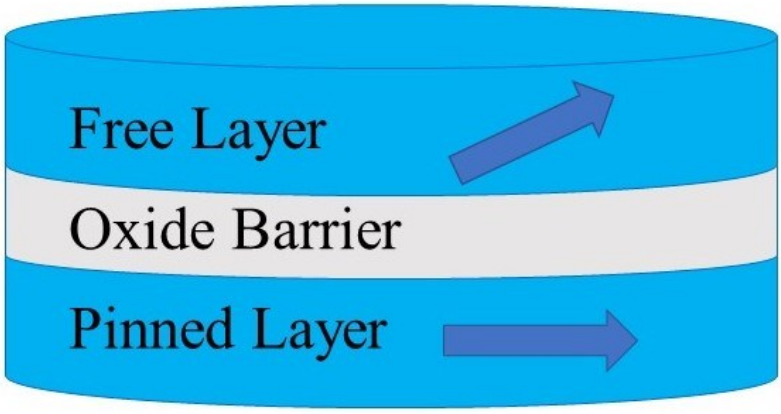

Figure 0.1 Basic structure of an MTJ

This device exhibits a difference in the resistance, depending on the mutual orientation of the magnetizations of the two magnetic layers, known as the tunnel magnetoresistance (TMR) effect. Another typical system is the Spin Hall geometry, which basic geometry is a bilayer structure of a magnetic material on top of a non-magnetic layer, usually a heavy metal (HM). One of the most interesting aspect of these devices is that their magnetization can be controlled and displaced from the equilibrium conditions by means of the electric current. This will be introduced in the next Chapter 1.

This thesis, by means of micromagnetic simulations, focuses on the design

of spintronic devices studying the MTJ, in particular aimed at logic and sensing applications, which are fundamental in the technological field. Moreover, a study on the dynamical behavior of a ferrimagnetic (FiM) material in a Spin Hall configuration, as alternative to MTJs, is micromagnetically analyzed.
This study has been performed by means of numerical simulations using the Petaspin micromagnetic solver[12], [13].

The structure of this dissertation is the following:

Chapter 1 the theoretical model and an overview of the most important physical phenomena relevant for the thesis are introduced in this part; these are the background required to understand the results presented in this thesis.
Chapter 2 An MTJ logic gate based on IMP and NOT operations is presented, which exploits the voltage controlled magnetic anisotropy to avoid the requirement of an external applied field.
Chapter 3 here, a magnetic field sensor based on the spintronic diode effect at low frequency is presented, along with its characterization.
Chapter 4 The characterization of the current-induced dynamics of a bilayer transition metal/rare earth ferrimagnet is discussed.
Chapter 5 it summarizes the results obtained in this thesis and outline the perspectives and future works that can be based on the current.

Chapter 1

1.Models

Magnetic dynamics induced by an electrical spin-polarized current is a phenomenon of high interest in the technology sector. The intent of the following section is to give an idea of the micromagnetic theory used in the results presented in this thesis, introducing the concept of numerical simulations, the equations exploited for describing the system under study and the terms of the motion equation.

1.1. Micromagnetic approach

Micromagnetism [7] is a theory for describing magnetic materials which treats them as a classical continuous medium, described by appropriate differential equations. The basics assumptions of this approach are that all the properties of the system are uniforms, the gradient of the magnetization vector slowly changes in time and space, and the length of magnetization vector is constant. The last assumption leads to the condition of temperatures far from the Curie temperature.

Otherwise inaccessible in real experiments, micromagnetic simulations allow to investigate some aspects of the magnetization dynamics, in order to study and design magnetic devices. The basic idea of the micromagnetic simulation approach is to integrate the appropriate differential equation numerically, using a spatial discretization. The dimension of the cells must

be small enough to consider uniform the properties of the system, but big enough to be able to take an average of the atomic properties as depictive of the material ones (the dimensions are usually between 1 nm and less than 10 nm).

The numerical method used is the finite difference (FD), which uses a regular shaped 3D mesh of orthorhombic cells to discretize the simulated area [14][15], such as in the following in Figure 1.1

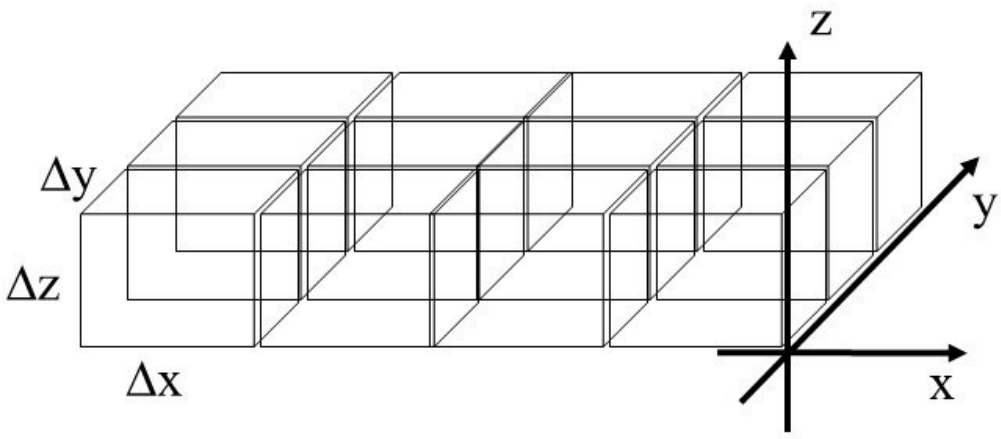

Figure 1.1 Schematics of the discretization for finite difference method

The method has as core the approximation of the partial derivatives of a function $f(\vec{r},t)$, dependent on space $\vec{r}$ and time t, by finite difference quotients $(\Delta x, \Delta y, \Delta z, \Delta t)$ such as

$$\frac{\partial f(x,y,z,t)}{\partial x} \cong \frac{f(x+\Delta x,y,z,t)-f(x,y,z,t)}{\Delta x} \tag{1.1}$$

The dynamical evolution of the system is obtained by the integration of the appropriate differential equation, which will be introduced in the next section 1.2, per each cell.

1.2. Landau-Lifshitz-Gilbert Equation (LLG)

A ferromagnetic material state is described by the vector of magnetic field $\overrightarrow{\mathrm{M}}(\vec{\mathrm{r}})$ which represents the local magnetization in each point in the considered material.

For ferromagnets, below the Curie point, at the smallest compatible spatial scale with the continuous hypothesis, the strong exchange interaction prevails on any other kind of force. The fundamental constraint which takes into account this is $\left|\vec{M}(\vec{r})\right| = M_s(T)$, which means that the modulus of the magnetization vector is equal to the magnetization saturation $M_s(T)$ at the temperature T.

The magnetization equilibrium states in the absence of any external stimulus, are described by the so-called Brown's equations[7], [16]

$$\begin{cases} \mu_0 M_s \overrightarrow{m} \times \vec{H}_{eff} = 0 \\ \left.\dfrac{\partial \overrightarrow{m}}{\partial \overrightarrow{n}}\right|_{\partial\Omega} = 0 \end{cases} \tag{1.2}$$

Where μ_0 is the vacuum permeability, $\overrightarrow{m} = \frac{\vec{M}}{M_S}$ is the normalized magnetization vector, $\partial\Omega$, is the body surface and $\overrightarrow{n}$ is the normal vector to the surface. The effective field $\vec{H}_{eff}$ *is* defined as $\vec{H}_{eff} = -1/(\mu_0 M_s)(\delta\varepsilon/\delta\overrightarrow{\mathrm{m}})$ where the ε is the energy density of the system and considers all the information of the geometry and the magnetic properties

of the system [17]. This term will be discussed in the following section 1.4. The equations (1.2) point the fact that the local torque exerted on the magnetization by the effective field and the derivative of $\overrightarrow{m}$ on the body surface must be null.

When $\mu_0 M_s \vec{m} \times \vec{H}_{eff} \neq 0$, the system is not at the equilibrium, and it will evolve.

A widely used equation for describing the effects of an evolving magnetic dynamics of a material is the Landau-Lifshitz-Gilbert (LLG) equation [18], [19]

$$\frac{\partial \vec{M}}{\partial t} = -\gamma \vec{M} \times \vec{H}_{eff} - \frac{\alpha}{M_s} \vec{M} \times \frac{\partial \vec{M}}{\partial t} \tag{1.3}$$

Where γ is the gyromagnetic ratio and α is the Gilbert's damping constant. By rewriting equation (1.3) and normalizing it by dividing both sides for γM_s^2, can be obtained

$$\frac{1}{\gamma\, M_s^2} \frac{\partial \vec{M}}{\partial t} = -\frac{1}{\gamma\, M_s^2} \gamma \vec{M} \times \left(\vec{H}_{eff} - \frac{\alpha}{\gamma\, M_s} \frac{\partial \vec{M}}{\partial t} \right) \tag{1.4}$$

Now, by introducing the normalized magnetization and the normalized effective field such as $\vec{m} = \frac{\vec{M}}{M_s}$, $\vec{h}_{eff} = \frac{\vec{H}_{eff}}{M_s}$ and by measuring the time in units of $(\gamma M_s)^{-1}$, the equation (1.4) can be expressed in the dimensionless form:

$$\frac{\partial \vec{m}}{\partial t} = -\vec{m} \times \left(\vec{h}_{eff} - \alpha \frac{\partial \vec{m}}{\partial t} \right)$$

(1.5)

It can be noticed how, written in this form, the LLG shows that the right member is equivalent to the subtraction from the effective field of a viscous term proportional to the time derivative of the magnetization. In particular, the term $\vec{m} \times \vec{h}_{eff}$ describes the precession of the magnetization around the axis identified by the effective field, while the term proportional to $\vec{m} \times \frac{\partial \vec{m}}{\partial t}$ describes the damping of the magnetization toward the equilibrium state, again identified by the effective field (see Figure 1.2 a sketch of the LLGS equation.

1.3. Effective field terms

In the discussion of the Landau-Lifshitz Gilbert equation, it is mentioned how the magnetization precession happens around the axis identified by the effective field. This term takes into account all the geometrical and magnetic contributions acting on the magnetization of the material, in which are linearly combined as $\vec{h}_{eff} = \vec{h}_{ext} + \vec{h}_{ex} + \vec{h}_{demag} + \vec{h}_{an} + \vec{h}_{DMI} + \vec{h}_{th}$, where the terms are external, exchange, demagnetizing, anisotropy, Dzyalonshinskii-Moriya interaction (DMI), and thermal fields, respectively. In this section the important contributions of the effective field for the results presented in this thesis will be discussed.

Zeeman Field

The Zeeman field takes into account the interaction between the external or applied field $\vec{h}$ and the magnetization of the system. In the limit of uniform field, it is simply calculated from the components of the external field [7][20].

The expression of the Zeeman field $\vec{h}_{ext}$ simply is

$$\begin{aligned}\vec{h}_{ext,x} &= \vec{h} \cdot \vec{u}_x \\ \vec{h}_{ext,y} &= \vec{h} \cdot \vec{u}_y \\ \vec{h}_{ext,z} &= \vec{h} \cdot \vec{u}_z\end{aligned}$$

(1.6)

Where $\vec{u}_x$, $\vec{u}_y$, $\vec{u}_z$ are the unity vectors.

Exchange Field

The exchange field takes into account the energy difference, due to the Coulomb repulsion and the principle of exclusion of Pauli, between the symmetric and antisymmetric spin states for the wave function of a spin ensemble expressed in the Heisenberg Hamiltonian [21], [22].

The expression of this term of the effective field is

$$\vec{h}_{ex} = \frac{2A}{\mu_o M_s^2} \vec{\nabla} \cdot \left(\vec{\nabla}\vec{m}\right)$$

(1.7)

Where A (J/m) is the exchange stiffness and depends on the material considered.

Demagnetizing Field

The demagnetizing (or magnetostatic) field takes into account the interactions existing in the material due to the magnetic dipoles, and can be derived from Maxwell's equations [20].
The expression of this term of the effective field is

$$\vec{h}_{demag} = -\vec{N} \cdot \vec{m} \tag{1.8}$$

Where $\vec{N} = diag(N_x, N_y, N_z)$ is the demagnetization tensor and depends on the shape of the simulated system.

Magnetic Anisotropy Field

The magnetic anisotropy field takes into account the energy difference that arises in some crystalline lattices, where the energy is lower for magnetization when it is parallel to certain crystallographic directions (easy axis) and it is higher in others (hard axis) [20], [23]. For a matter of interest, only the term of the uniaxial anisotropy will be considered.
The expression of this term of the effective field is

$$\vec{h}_{an} = \frac{2K_u}{\mu_0 M_s^2}(\vec{m} \cdot \vec{u}_i)\vec{u}_i \tag{1.9}$$

Where K_u (J/m^3) is the uniaxial anisotropy constant and $\vec{u}_i$ is the

direction of the uniaxial anisotropy.

An interesting effect to modify and control this term is the so called voltage controlled magnetic anisotropy (VCMA), where an applied voltage gives rise to a change of the perpendicular magnetic anisotropy[24][25], [26]. An interesting case is the one of a magnetic tunnel junction with a voltage applied to its terminals. In this case, K_u can be substituted by the normalized effective anisotropy constant k_{eff} [27], which takes into account the effect of contribution of the voltage and the anisotropy

$$k_{eff} = \frac{2K_u}{t_{FL}\mu_0 M_s^2} - \frac{2\xi V}{M_S t_{FL} t_{OX}}$$

(1.10)

where V is the applied voltage, ξ $(J/V \cdot m)$ is the magneto-electric coefficient, t_{FL} and t_{OX} are the thicknesses of the MTJ's free layer and oxide.

Dzyalonshinskii-Moriya Interaction field

Dzyalonshinskii-Moriya interaction field, also known as antisymmetric exchange, takes into account the energy term due to the lack of inversion symmetry along with the spin-orbit coupling [28], [29].
The expression of this term of the effective field [30]–[32] is

$$\vec{h}_{DMI} = -\frac{2D}{\mu_0 M_s^2}(\vec{u}_z\,(\nabla \cdot \vec{m}) - \nabla \vec{m}_z)$$

(1.11)

where D is the IDMI parameter accounting for the strength of the interaction.

Thermal Field

The thermal field takes into account the effect of the temperature in a device in a stochastic way. In each computational cell, the effect of temperature can be expressed as

$$\vec{h}_{th} = \frac{\vec{\chi}}{M_s}\sqrt{\frac{2\alpha \quad k_B T}{\mu_0 \gamma_0 \Delta V M_s \Delta t}}$$

(1.12)

with k_B being the Boltzmann constant, ΔV the volume of the computational cubic cell, Δt the simulation time step, T temperature of the sample, and $\vec{\chi}$ a three-dimensional white Gaussian noise with zero mean and unit variance[33], [34]. This noise is assumed to be uncorrelated for each computational cell.

1.4. Current-induced torque terms

Initially proposed independently by Slonczewski [35] and Berger [36], spin-torque describes the action of incoming itinerant electrons on localized magnetic moments in a magnetic material. The basic idea is that an electrical current, polarized in spin, by some undergoing physical effect, exerts a torque on the magnetization vector, acting like an anti-damping term (see Figure 1.2 a sketch of the LLGS equation, that can compensate, overcome or less the damping term [36]. The interesting technological application about this torques is that, based on in which state

the system is, they can switch the magnetization or make it precede [37], [38].

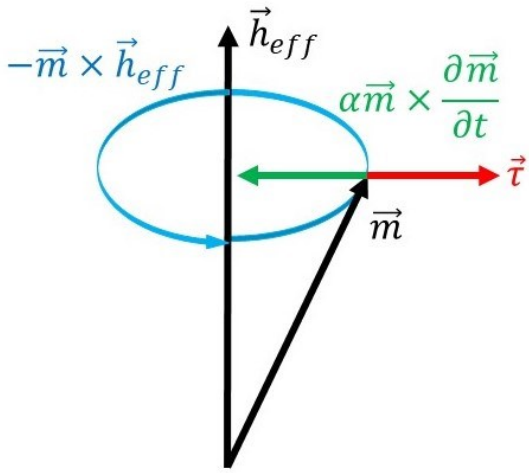

Figure 1.2 a sketch of the LLGS equation, with the various contributions. In light blue, the magnetization $\vec{m}$ precession around $\vec{h}_{eff}$, in green the effect of the Gilbert damping and in red the effect of the torque $\vec{\tau}$

The most common implementation of spin torques is to add a direct torque term into the standard LLG equation (1.5), often called the Landau–Lifshitz–Gilbert–Slonczewski (LLGS) equation [36], i.e.

$$\frac{\partial\vec{m}}{\partial t} = -\vec{m} \times \vec{h}_{eff} + \alpha\vec{m} \times \frac{\partial\vec{m}}{\partial t} + \vec{\tau} \tag{1.13}$$

Where $\vec{\tau}$ is the Slonczewski-like torque and will be discussed in the following subsections.

Spin transfer torque

The Spin-Transfer Torque effect happens when an electric current flows in a magnetic multilayer [35] constituted at least of two ferromagnetic layers divided by a spacer, such as in a magnetic tunnel junction or in a spin valve, or in two magnetic domains divided by a domain wall. When the current flows through a FM layer or a domain, it becomes spin polarized, so there is a spin current in addition to the electric current. When the electric current goes into another FM layer or another domain, electrons become aligned along the new magnetization direction. Because of the angular momentum ought to be conserved, there must be a spin (angular momentum) transfer between spin-polarized conduction electrons and magnetic lattice.

While the STT is constituted by two types of contributions, an out-of-plane contribution, that acts when the current flows perpendicularly to the plane of a multilayer, and an in-plane contribution, such as when the current flows in the plane of a magnetic material through a domain wall, for sake of brevity only the out-of-plane will be considered, because it is the only one of interest in this work.

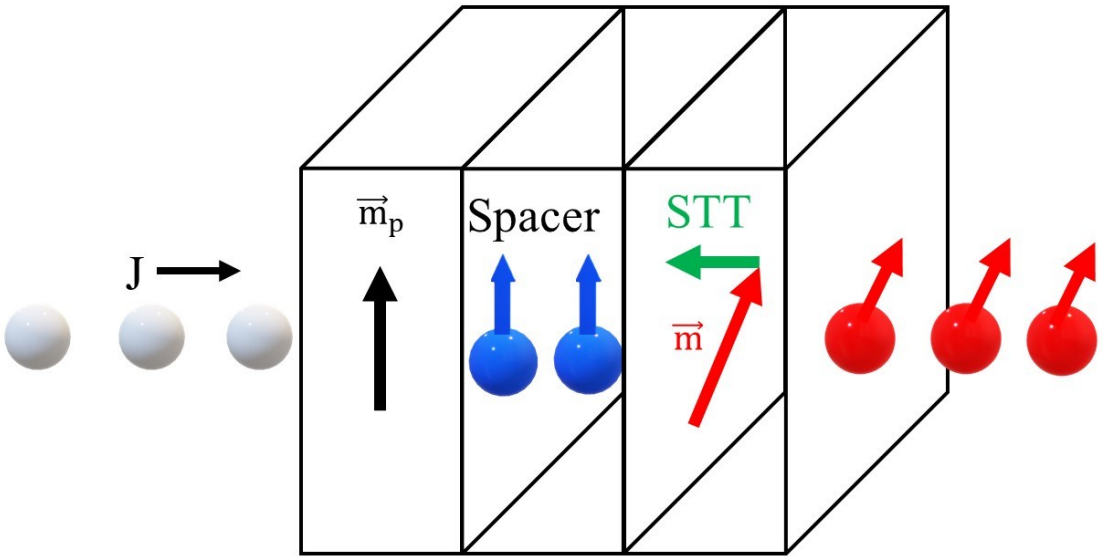

Figure 1.3 schematic picture of the STT arising in a FM/Spacer/FM bilayer.

At this point, the STT contribution to the LLGS equation (1.13), τ_{STT}, is the following [39], [40]

$$\tau_{STT} = -\sigma\left[\vec{m} \times \left(\vec{m} \times \vec{m}_p\right)\right] \tag{1.14}$$

$\sigma = J\sigma_\perp/(1+\eta^2 \cos\beta)$ is the current torque proportionality coefficient, where η is the spin-polarization factor, which takes into account the fraction of electrons polarized in spin and $\beta = \arccos\left(\vec{m} \cdot \vec{m}_p\right)$ is the angle between the free layer magnetization, *i.e.* the layer, which is reoriented by STT, and pinned layer magnetization $\vec{m}_p$, *i.e.* the layer which polarizes the charge current, (see Figure 1.3), $\sigma_\perp = (2\eta g\mu_B)/(2\gamma e\, M_s^2 t_{FL})$, where g is the Landé factor, $\mu_B$is the Bohr magneton, e is

the electron charge and t_{FL} is the free layer thickness.

Spin orbit torque

The Spin Orbit Torque (SOT) effect appears in all those systems where a spin orbit coupling and a lack of inversion symmetry appear. While this torque can be generated from various types of effects, such as the Rashba-Edelstein effect [41], [42], the orbital Hall effect [43], [44] or the thermal generated SOT [45], for sake of brevity it will be discussed only the Spin Hall Effect (SHE), which is the one of interest for the work presented in this thesis. The SHE is a spin orbit coupling effect that has its origin in the bulk of a material. If a spin unpolarized charge current is injected in the plane of a layer, that can be an heavy metal (HM), such as aluminum or platinum [46], [47], it is converted into a pure spin current in the transverse direction. This effect was predicted in 1971 D'Yakonov and V. I. Perel'[48]. This asymmetric scattering leads to spin-up and spin-down electrons being deflected in opposite directions (Figure 1.4 schematic picture of the SHE arising in a FM/HM bilayer) and generates a transverse spin current at the surface of the HM. This creates a spin accumulation, *i.e.*, a difference between spin-up and down population at the interface between a heavy metal and a magnetic material, (such as a ferromagnet or ferrimagnet (FiM)). This uncompensated population of spin-polarized electrons, passing through the magnetized material, exerts a torque on its magnetization.

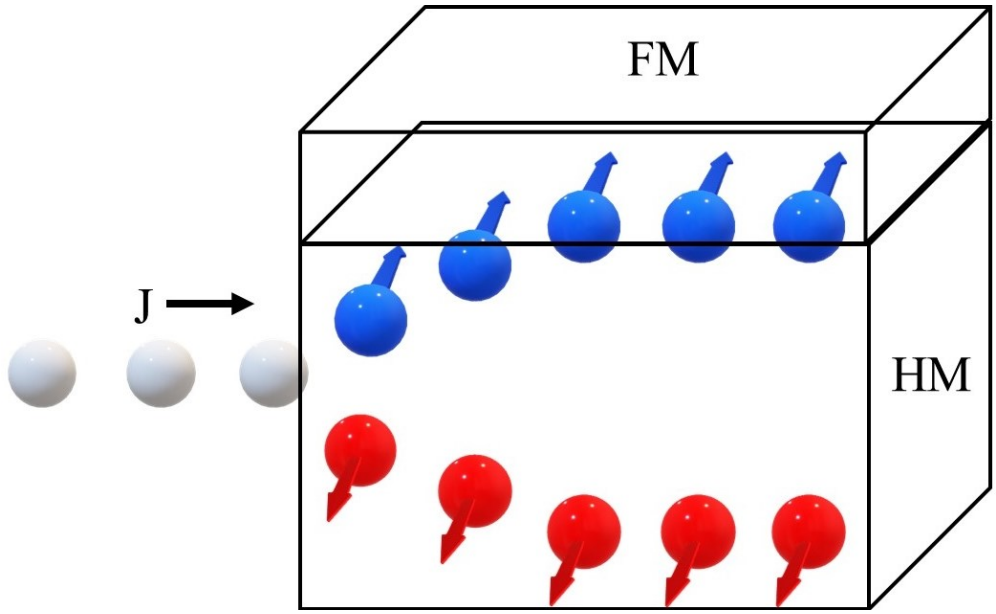

Figure 1.4 schematic picture of the SHE arising in a FM/HM bilayer

At this point, the SHE contribution to the LLGS equation (1.13), τ_{SH}, is the following

$$\tau_{SH} = H_{SH}\vec{m} \times (\vec{m} \times \vec{p}) \tag{1.15}$$

with $\vec{p}$ being the direction of the spin current polarization and $H_{SH,i} = \gamma(\hbar\theta_{SH}J)/(2ed\mu_0 M_S)$ its amplitude. $\hbar$, J and d are the reduced Planck's constant, the in-plane injected current and magnetic layer thickness, respectively. θ_{SH} is the spin Hall angle, which takes into account how efficiently the HM converts the current of electric charges into spin current [49].

1.5. Two sublattices model

Albeit powerful in the description of the dynamics in ferromagnets, the

model previously presented lacks in applicability to describe other systems such as ferrimagnets and antiferromagnets (AFM). For FMs the minimum energy configuration occurs for parallel spins, so the dynamics could be described by associating to each cell a single spin vector. Now, in AFMs and FiMs the interaction between the atoms is such as to create a minimum energy configuration when the spins are antiparallel. In the first kind of material, the opposing magnetic moments are equal in magnitude, while they are unequal in second ones. This results in a zero or non-zero net magnetization respectively for AFMs and FiMs.
These antiparallel magnetic moments cannot be described as before. This is because a similar model would not respect the micromagnetic basic assumptions of uniformity of properties and small changes in the magnetization gradient. In the micromagnetic approach the AFM/FiM order could be described by means of the magnetizations of two different sublattices, $\vec{m}_1$ and $\vec{m}_2$, which reflect the average magnetization of the spins within the same discretization cell.

The equations which describe the dynamics of this system are dual coupled LLG equations with Slonczewski-like torque τ [13]

$$\begin{aligned}\frac{d\vec{m}_1}{dt} &= -\gamma_1 \vec{m}_1 \times \vec{H}_{eff,1} + \alpha \vec{m}_1 \times \frac{d\vec{m}_1}{dt} + \tau_1 \\ \frac{d\vec{m}_2}{dt} &= -\gamma_2 \vec{m}_2 \times \vec{H}_{eff,2} + \alpha \vec{m}_2 \times \frac{d\vec{m}_2}{dt} + \tau_2\end{aligned} \qquad (1.16)$$

In this coupled equations, all the contributions in the effective fields keep the same definition for each sublattice but the exchange field.

In this model, the exchange interaction becomes more complex and it is given by three contributions: homogeneous interlattice exchange (Figure 1.5a), inhomogeneous interlattice exchange (Figure 1.5b), and inhomogeneous intralattice exchange (Figure 1.5c)[50][51]. Their strengths are characterized by three parameters A_0, A_{12}, and $A_{11} = A_{22}$ respectively. The exchange field can be written as

$$\vec{h}_{exch,i} = \frac{1}{\mu_0 M_{s,i}^2}\left(2A_{11}\,\nabla^2\,\vec{m}_{\mathrm{i}} + \frac{4A_0}{a^2}\vec{m}_{\mathrm{j}} + A_{12}\,\nabla^2\,\vec{m}_{\mathrm{j}}\right) \tag{1.17}$$

with a being the lattice constant and $M_{s,i}$ is the magnetization saturation of the sublattice i = 1,2.

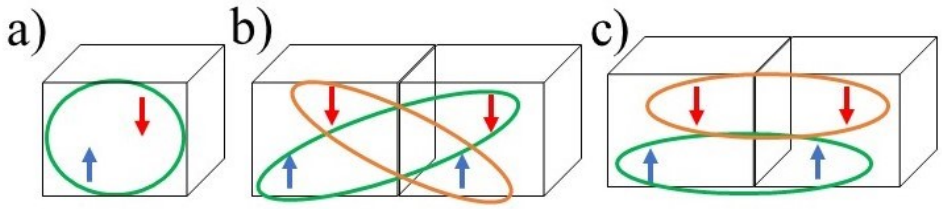

Figure 1.5 Example of a discretization cubic cell characterized by two-sublattice magnetizations for a FiM/AFM with a sketch of the contribution for the exchange interaction (a) homogeneous interlattice exchange, (b) inhomogeneous interlattice exchange, and (c) inhomogeneous intralattice exchange

It worth noticing that this model is completely capable of describing FiM, AFM and FM just changing the exchange parameters opportunely.

Chapter 2

2.Field-Free Magnetic Tunnel Junction for Logic Operations Based on Voltage-Controlled Magnetic Anisotropy*

In this chapter, a micromagnetic characterization and demonstration of an MTJ-based logic gate is shown. A series of two MOSFETs and two MTJs is chosen as basic structure to perform operations. The first ones operate as access devices, while the second ones perform the logic and store the output through their magnetization state. The configuration is specular, and the logic unit is composed of one MOSFET and one MTJ. The IMP and NOT logic operations are the complete logic base chosen to reproduce all the others logic operations. All of this can be performed without any external magnetic field by supplying a DC voltage to the circuit structure. The solution covered in this chapter is a proposal for higher energy-delay efficiency and better integration density than conventional CMOS-based computational architectures.

* Adapted from F. Cutugno, E. Garzón, R. De Rose, G. Finocchio, M. Lanuzza and M. Carpentieri, "Field-Free Magnetic Tunnel Junction for Logic Operations Based on Voltage-Controlled Magnetic Anisotropy," in *IEEE Magnetics Letters*, vol. 12, pp. 1-4, 2021, Art no. 4503904, doi: 10.1109/LMAG.2021.3118562.

2.1. Introduction

In the last years, the problems related to the big data computation requirements have rendered the state-of-art von-Neumann machines inefficient in terms of energy due to the well-known von-Neumann architecture bottleneck [52], [53]. In fact, the emerging applications like artificial intelligence, Internet of things, etc., demand a large number of off-chip memories to handle large data workloads. Due to the technology scaling that, up to now, has improved the efficiency of logic more than the efficiency of the data transfer, one of the most energy consuming operation is the energy required to communicate, that dominates on computation energy [54]. Magnetic Tunnel Junctions devices are an emerging and attractive technology for building logic configurations because computation is performed within the memory array (in-memory computing), combining the nonvolatile memory and logic circuits. This allows to improve both speed and energy consumption without the need of transferring the operation data to another memory cell or to another logic gate. This is a promising solution to increase the computing efficiency by avoiding the bottleneck problem.

Material implication (IMP) is a fundamental two-input Boolean logic operation (A → B) that reads "A implies B" or "if A, then B" and is equivalent to "(NOT A) OR B" [55], and it was classified as one of the four basic logic operation (with AND, NOT and OR) [56]. Moreover, the IMP and NOT logic operations can be combined to form a functionally complete set for Boolean algebra and all the others logic functions can be realized[57].

The system presented in this chapter allows to perform IMP and NOT logic operations by exploiting the tradeoff between the spin current and the voltage controlled magnetic anisotropy (VCMA) [58] in a scheme with two series-connected MTJs with a perpendicular magnetization. Differently from prior work [59], the micromagnetic simulations show that the logic operations can be performed without any external magnetic field, which is a key element for easier integration with CMOS technology and a better scalability of the device. The external field can be avoided due to the choice of the device geometry exploiting an elliptical shape that breaks the in-plane symmetry.

2.2. Device and Micromagnetic details

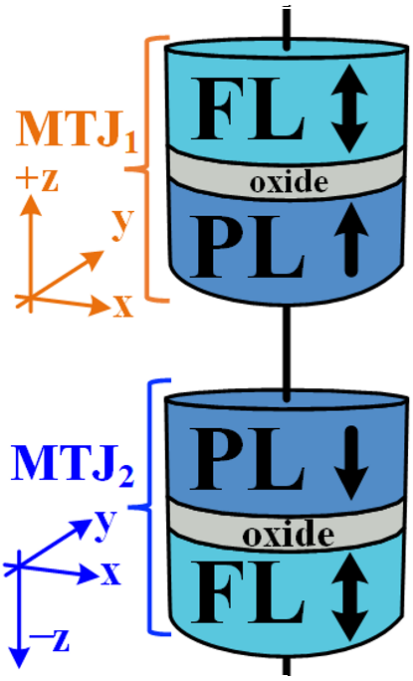

Figure 2.1 MTJ sketch and axis reference frame, where the free layer (FL) and the pinned layer (PL) are indicated.

For the micromagnetic simulation, two MTJs with perpendicular

magnetization are used to ensure higher thermal stability, lower power and better scalability compared to their in-plane counterparts [60]–[62]. The two MTJs have the pinned layers posed in a mirrored configuration (see Figure 2.1), *i.e.*one along +z and one along -z, and are called respectively MTJ_1 and MTJ_2.

The MTJs feature an elliptical geometry (60nm×30nm) with free layer thickness (t_{FL}) of 1 nm and oxide thickness (t_{OX}) of 1 nm, as illustrated in the following Figure 2.2.

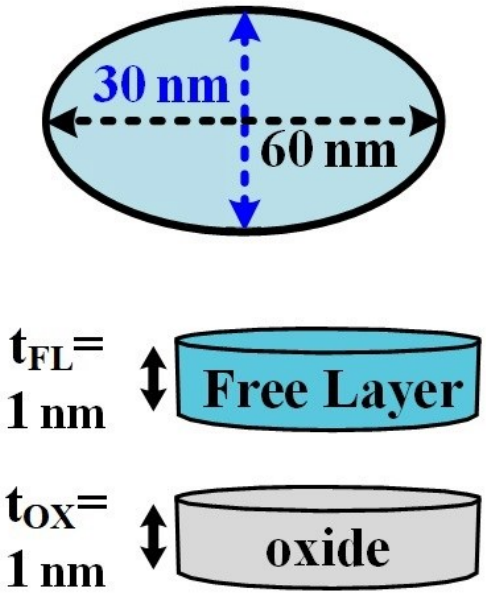

Figure 2.2 Geometrical dimensions of the p-MTJs: top-view with the axis length, and thickness of the free layer and oxide barrier

The magnetic parameters used in our analysis, referring to a CoFeB free layer, are: saturation magnetization M_S=950×10^3 A/m, exchange constant A=2.0×10^{-11} J/m, magnetic damping α_G = 0.02, and perpendicular anisotropy constant of the magnetic material K_u = 0.60 MJ/m^3. The resistance-area product is 10 Ω·μm^2 [63] whence the resistance values for the parallel and antiparallel case are R_P= 7.074 kΩ and R_{AP}=17.684 kΩ

corresponding to a TMR of 150%.

The truth tables of the implemented IMP and NOT logic operations, are shown in the following Table 1, where R_P and R_{AP} correspond to bit '0' and bit '1', respectively, and "ini" and "fin" are the initial and final states of the MTJs.

IMP			
$MTJ_{1,\,ini}$	$MTJ_{2,ini}$	$MTJ_{1,\,fin}$	$MTJ_{2,fin}$
R_P	R_P	R_P	R_{AP}
R_P	R_{AP}	R_P	R_{AP}
R_{AP}	R_P	R_{AP}	R_P
R_{AP}	R_{AP}	R_{AP}	R_{AP}
NOT			
MTJ_{ini}		MTJ_{fin}	
R_P		R_{AP}	
R_{AP}		R_P	

Table 1 Truth tables of the IMP and NOT logic operations reporting the initial and final states of the two MTJs.

Recalling equations (1.9) and (1.10), the contribution of the VCMA is $H_{VCMA} = -\frac{2\xi V_{MTJ}}{M_S t_{FL} t_{OX}}$, where the magneto-electric coefficient ξ is considered equal to 500 f*J*/(V·m) [64] and $V_{MTJ} = R_i \cdot I$, with $i = P, AP$ where the resistance considered is the parallel or antiparallel case depending on the initial state, and I is the electrical current.

Last introductory note, in this analysis, the magnetization is considered

switched when the normalized *z*-component of the magnetization reaches the value of |0.9|, with opposite sign respect to the initial one.

2.3. IMP Logic Operation

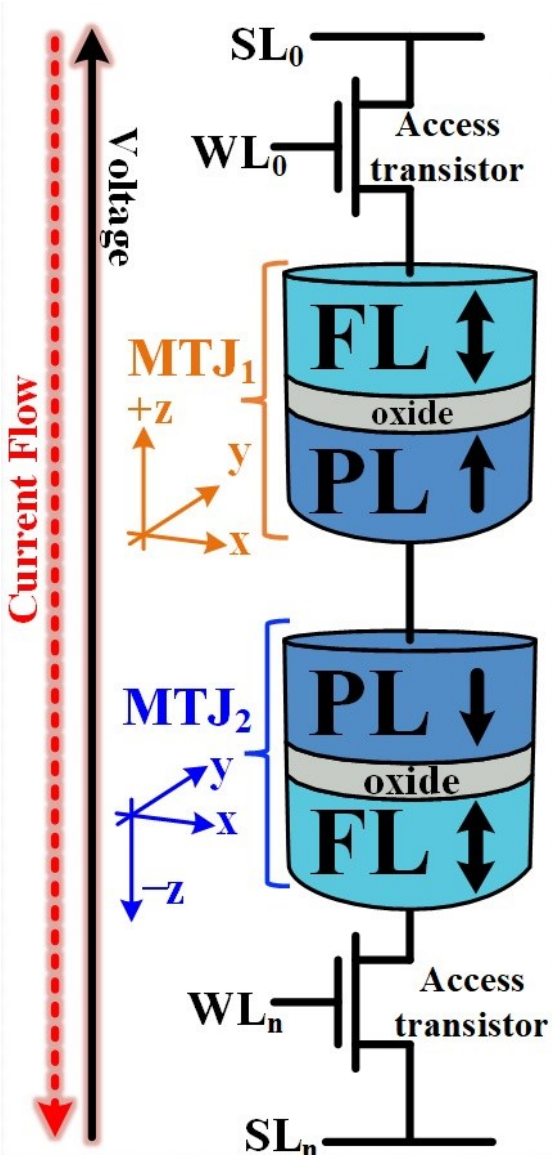

Figure 2.3 A schematic of the logic unit composed of two perpendicular MTJs and two CMOS access transistors in series connection with the indication of the voltage and current direction for the IMP

As it can be seen in truth table (Table 1), the IMP operation requires two

MTJs to operate. In this operation, the magnetization state has to switch only for the first input combination, *i.e.*, the MTJ_2 must change its state from parallel (0) to antiparallel (1). In all other cases, the initial magnetization state of both MTJs must remain unchanged after the pulse current to ensure proper operation. Here, the logic gate is composed of a stack with two access transistors and two MTJs in a mirrored geometry. In Figure 2.3, other than the gate, also the current flow and the applied voltage is shown. It worth noting that the sign of the current/voltage is opposite in the two MTJs due to the specular geometry. In fact, the order of the trilayers, as well as the direction of the pinned layers magnetizations, define how the effect of the STT acts on the FL. In the MTJ_1 the current enters the FL and exits the PL, vice versa in the MTJ_2 it enters the PL and exits the FL, although with the same amplitude due to the series connection. In Table 2, the resistance of MTJs, the required current for operating and the relative effective field term due to VCMA are tabulated.

IMP Input combination	**MTJ_1 Res (Ω)**	**MTJ_2 Res (Ω)**	**Current *I* (μA)**	**Current density *J* (MA/cm^2)**	**H_{VCMA} MTJ_1 (mT)**	**H_{VCMA} MTJ_2 (mT)**
Case 1 - (0,0)	7074	7074	9.19	0.65	68.4	-68.4
Case 2 - (0,1)	7074	17685	5.65	0.40	42.1	-105.3
Case 3 - (1,0)	17685	7074	5.65	0.40	105.3	-42.1
Case 4 - (1,1)	17685	17685	3.96	0.28	73.7	-73.7

Table 2 Resistance, current and VCMA required in IMP operation

In this work, the uniaxial anisotropy has to be high enough to fix the

magnetization of the free layer along z. In fact, a too low anisotropy would let the FL magnetization relax in the plane xy, nullifying the advantages of having a perpendicular MTJ, as shown in Figure 2.4 where the simulations are performed without uniaxial anisotropy.

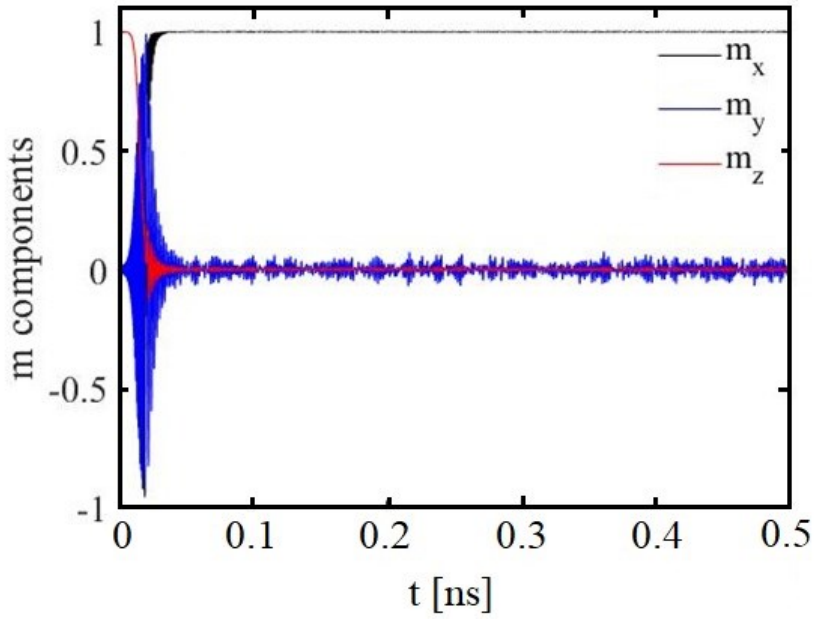

Figure 2.4 relaxation of the magnetization components without the uniaxial anisotropy.

Similarly, the anisotropy cannot be too large, or the VCMA would not be able to assist or avoid the switching between the two states of the FLs (parallel or antiparallel). In fact, the effect of the applied voltage is to increase (decrease) the energy barrier of the MTJ_1 (MTJ_2) due to the VCMA effect, and, at the same time, to avoid the application of an external magnetic field. About the current, it gives rise to an efficient way to manipulate the magnetic configuration maintaining a large magnetic stability in a static state through the STT effect, as already mentioned. In fact, depending on the initial configuration, STT may switch or left unperturbed the magnetization state. The combination of these two effects

and specular geometry are the key for the logic gate.

The dynamics of the m_z for both MTJs when performing the IMP operation for all the four input combinations is shown in Figure 2.5. From Figure 2.5(a), referring to the first input combination, the MTJ_1 keeps its initial state, whereas the MTJ_2 changes its state from 0 to 1 after 14.1 ns.

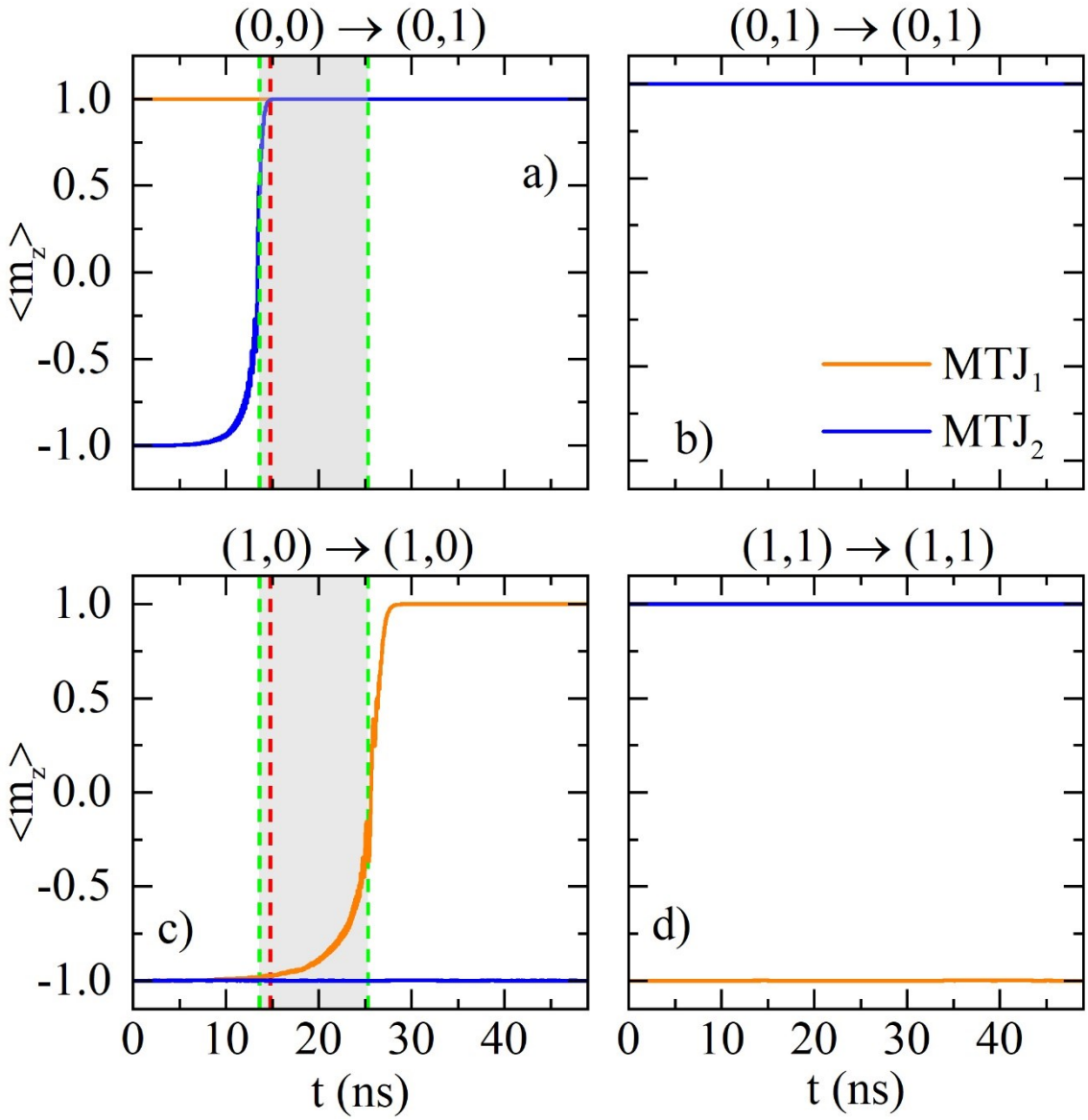

Figure 2.5 Dynamics of the m_z component for MTJ1 (orange) and MTJ2 (blue) during the IMP operation in the cases of (a) IMP(0,0), (b) IMP(0,1), (c) IMP(1,0), and (d) IMP(1,1). The dashed green lines delimit the operating area (in grey) of the device. The dashed red line represents the optimal operating value for the NOT operation.

In Figure 2.6, the 3-dimensional magnetization dynamics shows that the switching occurs following a circular orbit with uniform spatial magnetization.

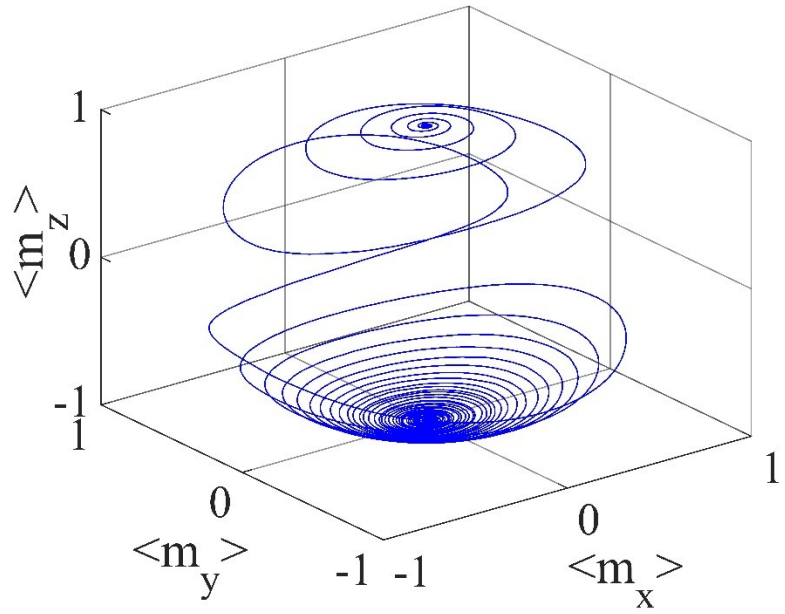

Figure 2.6 3d dynamics of the magnetization for the state (0,0) → (0,1).

The results obtained for the other three input combinations are shown in Figure 2.5 (b)-(d). From Figure 2.5 (b) and (d), both MTJs preserve their initial state after a 50-ns applied pulse. Conversely, in the case of the third input combination, the MTJ_1 changes its state after 27.2 ns, as shown in Figure 2.5 (c). This is in contrast with the truth table of Table 2, which gives some limits to design the geometry and to the current pulse length. Nonetheless, the switching time larger than the first case provides a sufficiently large margin in setting an appropriate pulse duration to guarantee the correct operation of the logic unit. In this study, this is achieved by applying a current pulse longer than 13.6 ns to ensure MTJ_2

switching for the first input combination, but at the same time shorter than 25.3 ns to avoid MTJ_1 switching for the third input combination.

2.4. NOT Logic Operation

Since the NOT is a 1-bit operation, the considered scheme is based on a single device composed by the MTJ_1 and the first CMOS access transistor connected in series. In particular, a voltage to the MTJ_1 is applied, as shown in Figure 2.7.

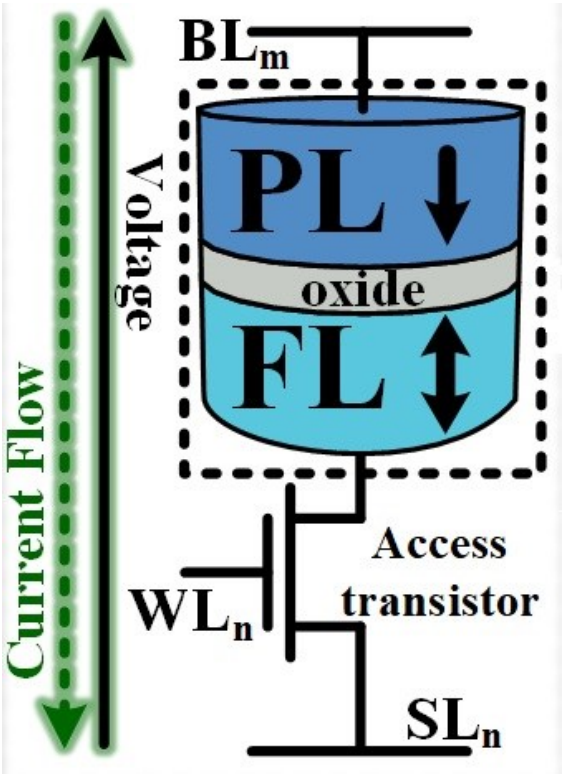

Figure 2.7 A schematic of the logic unit composed of one perpendicular MTJ and one CMOS access transistors in series connection with the indication of the voltage and current direction for the NOT operation.

In this logic gate, the key ingredient to perform the NOT logic operation without the assistance of an external magnetic field is the shape

anisotropy. The elliptical geometry of the considered device (see Figure 2.2) allows to start the magnetization precession during the NOT operation. In fact, it provides a sufficiently high shape anisotropy that acts as an in-plane field, that triggers the magnetization oscillation around the z-axis without the requirement of an external field.

In this study, to perform the NOT operation, the applied current density is -0.75 MA/cm^2, providing a VCMA field of about 197 mT (Table 3).

NOT	**MTJ_1 Res (Ω)**	**Current *I* (μA)**	**Current density *J* (MA/cm^2)**	**H_{VCMA} MTJ_1 (mT)**
NOT (0)	7074	-10.60	-0.75	-79.0
NOT (1)	17685	-10.60	-0.75	-197.4

Table 3 Resistance, current and VCMA required in NOT operation

An observation that deserves to be made is the following. The NOT operation can be performed without any information about the initial magnetization state (0 or 1). This means that checking the initial state of the NOT is not required to perform it. This makes quicker and simpler to perform the other logic operations, that are obtained by the combination of the NOT and the IMP.

The NOT(0→1) operation is described in Figure 2.8(a) and (b). As shown in Figure 2.8(a), after the application of the pulse current, the switching is complete after 14.4 ns. Figure 2.8 (b) shows the magnetization, which starts to oscillate in a uniform way following a 360° counterclockwise rotation around the *z*-axis with increasing trajectory amplitude. Once achieved the in-plane magnetization rotation, the magnetization reverses very quickly. Vice versa, a different behavior occurs for the NOT (1→0)

operation. In fact, starting from the antiparallel magnetization state, the VCMA triggers the magnetization oscillation with large amplitude of the *z*-component given by a trade-off between the applied current and the VCMA. In this case, the possibility to obtain 0 or 1 as final magnetization state depends on the switch off time of the current pulse. Here, if the current pulse is switched off during the negative semi-period values of the m_z oscillation, the magnetization moves toward the 1 state. Instead, switching off the current during the positive semi-period leads to a final 0 state. So, for the two switching cases, the magnetization dynamics is completely different depending on the initial state. In particular, Figure 2.8 (c)-(d) and (e)-(f) show two different NOT(1) operation when the current pulse is switched off at 13.9 and 14.8 ns, respectively. In fact, depending on the switch-off time during the semi-period positive of the oscillation, the magnetization dynamics can be uniform or not-uniform. In particular, if the pulse current is switched off far from the oscillation positive peak (for the considered oscillation the positive peak occurs at 14.8 ns) the switching is not-uniform, if the pulse current is turned off at the maximum positive value (or very close) of the magnetization oscillation the switching will be uniform.

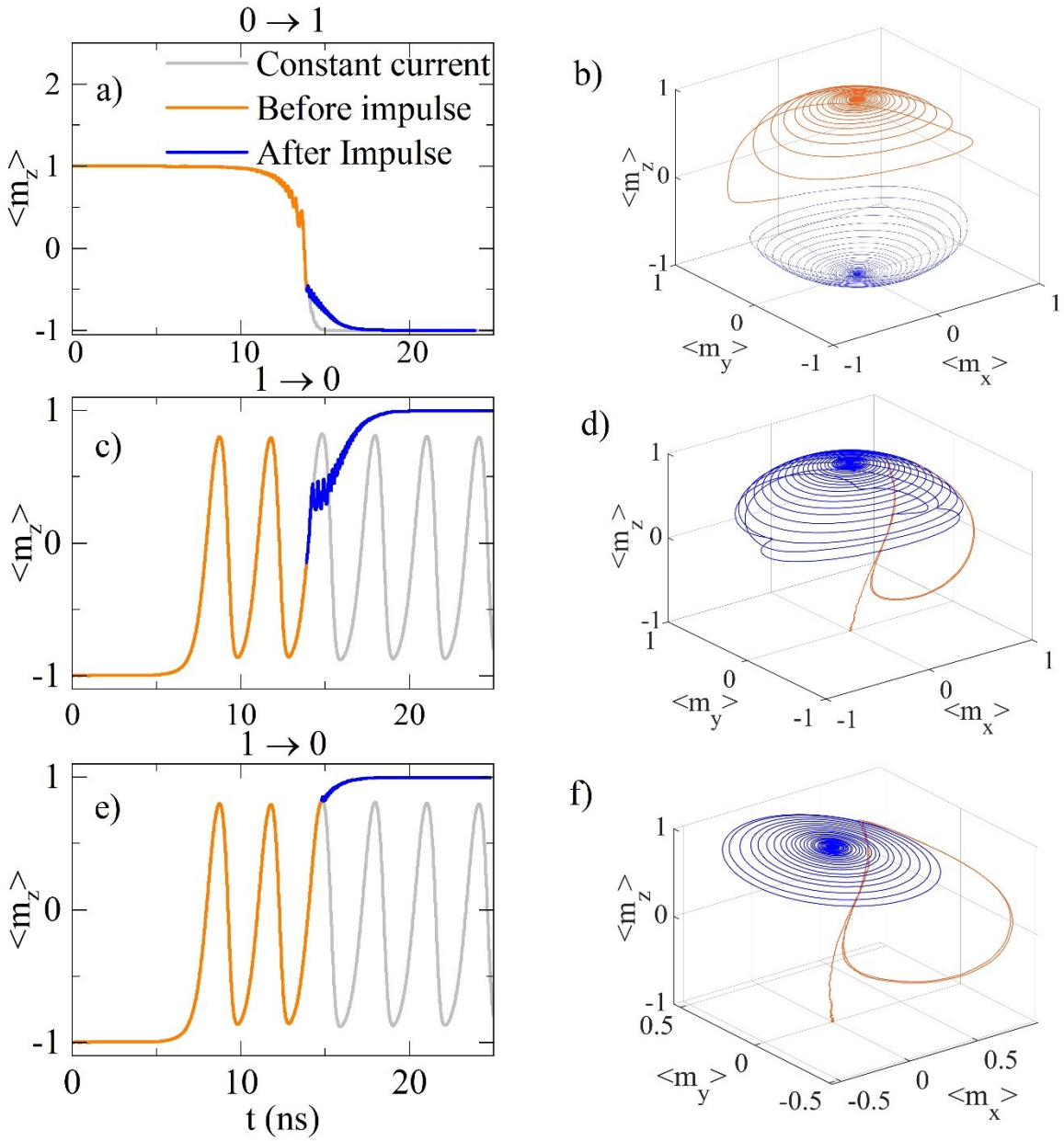

Figure 2.8. Dynamics of perpendicular MTJs m_z-component for the NOT operation. (a)-(b) Case NOT(0), where the curve depicts the trend before (orange) and after (blue) shutting off the current pulse at 13.9 ns and the relative 3d dynamics curve of the magnetization. (c)-(d) and (e)-(f) refer to the case NOT(1), where the curves depict the trend before (orange) and after (blue) shutting off the current pulse at 13.9 ns and 14.8 ns, respectively. Here, the grey curve is the persistent oscillation condition in which the current is kept constant throughout the time dynamics of the three magnetization components.

Figure 2.9 shows the snapshots of the magnetization at fixed times during (a) NOT(0) with current pulse duration of 13.9 ns, (b) NOT(1) with current pulse duration of 13.9 ns, and (c) NOT(1) with current pulse duration of 14.8 ns. As shown, in the case (a) and (c), the switching of the magnetization is uniform. When the current pulse is switched off far from the positive peak of the magnetization oscillation (13.9 ns, case (b)), the switching occurs following a non-uniform spatial distribution of the magnetization with the formation of a domain wall that extends in and out from the sample.

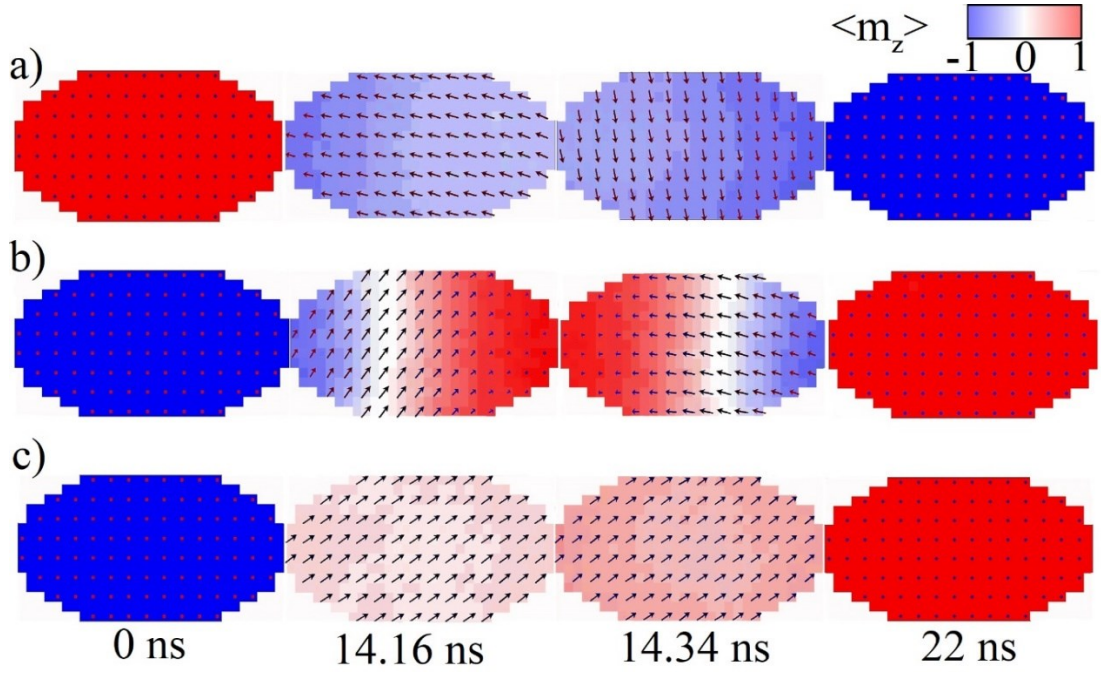

Figure 2.9 Magnetization snapshots for different times (0, 14.16, 14.34, and 22 ns) in the case of (a) NOT(0) with current pulse of 13.9 ns, (b) NOT(1) with current pulse of 13.9 ns, (c) NOT(1) with current pulse of 14.8 ns.

From this analysis, it can be concluded that NOT operation can be performed on a single device. When a pulse current is switched-off during the positive semi-period, e.g., between 13.9 and 15.2 ns in this study, the NOT operation is properly carried out regardless of the initial

magnetization state. With regards to the device-to-device variations of the proposed logic gates, it is obvious how, in all the operations discussed, NOT(1) is the most delicate operation to perform. Anyway, by considering a variation of 1% of the current amplitude with respect to the value used previously (J=0.75 MA/cm2), as shown in Figure 2.10 below, the NOT(1) operation is still working. However, it is expected that a correct and robust current pulse timing could be obtained by asserting proper values for both CMOS technology (width, length, etc.) and MTJ devices (VCMA coefficient, oxide thickness, dimensions, etc.).

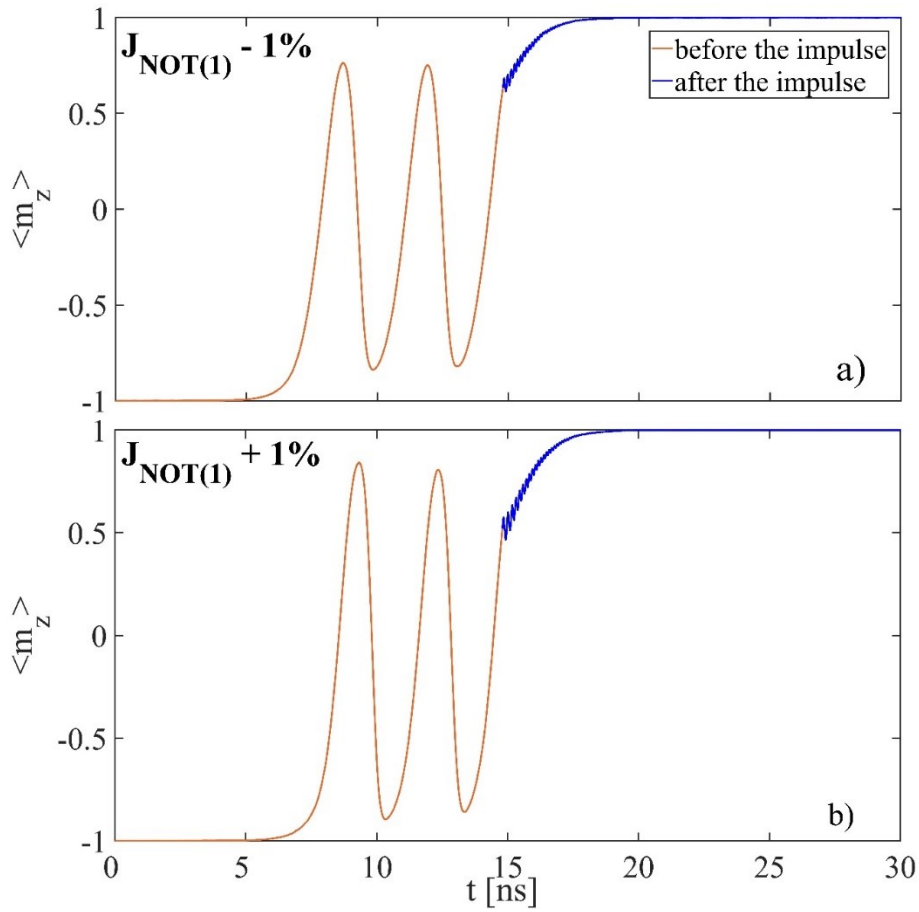

Figure 2.10 – NOT(1) considering the same parameters used previously but current values of J=0.7425 and J=0.7575 MA/cm²

It is worth noting how, in these results, the effect of the dynamical change

of the resistance is not considered. This could affect the magnitude of the applied current or voltage, changing the time of operation for the logic gates and the range of currents/voltages that allow the system to correctly perform the operations. Here, this effect is supposed negligible, because of the applied input is large enough to initiate the interested dynamics. Taking it into consideration is only a matter of calibration of the applied input. In an actual device implementation, this effect could be taken into account by a careful calibration.

2.5. Energetic Evaluation

Finally, the energetic evaluation of this work is resumed in Figure 2.11, that shows the Boolean logic functions based on IMP and NOT operations, along with their energy consumption. From Figure 2.11 (a), seven logic gates are presented and classified according to the number of cycles. Using the 1-cycle logic gates (i.e., IMP and NOT), a complete set of universal Boolean gates can be performed, being these the [OR, NIMP, NAND] and [AND, NOR] for the 2- and 3-cycle operations sets, respectively. Figure 2.11 (b) shows the average energy consumption per bit for the complete set of logic gates. The NOT operation exhibits energy consumption higher than IMP operation due to the required higher switching current (see Table 2 and Table 3). A nominal supply voltage V_{DD} = 0.9 V with a latency of 14 ns is assumed, which ensures a correct operation for the IMP and NOT operations, as shown in Figure 2.5 and Figure 2.8. It is worth pointing out that the choice of V_{DD} is based on simulations using a commercial 65-nm CMOS technology with Cadence Spectre. Therefore, the V_{DD} can easily

provide the current values reported in throughout this work.

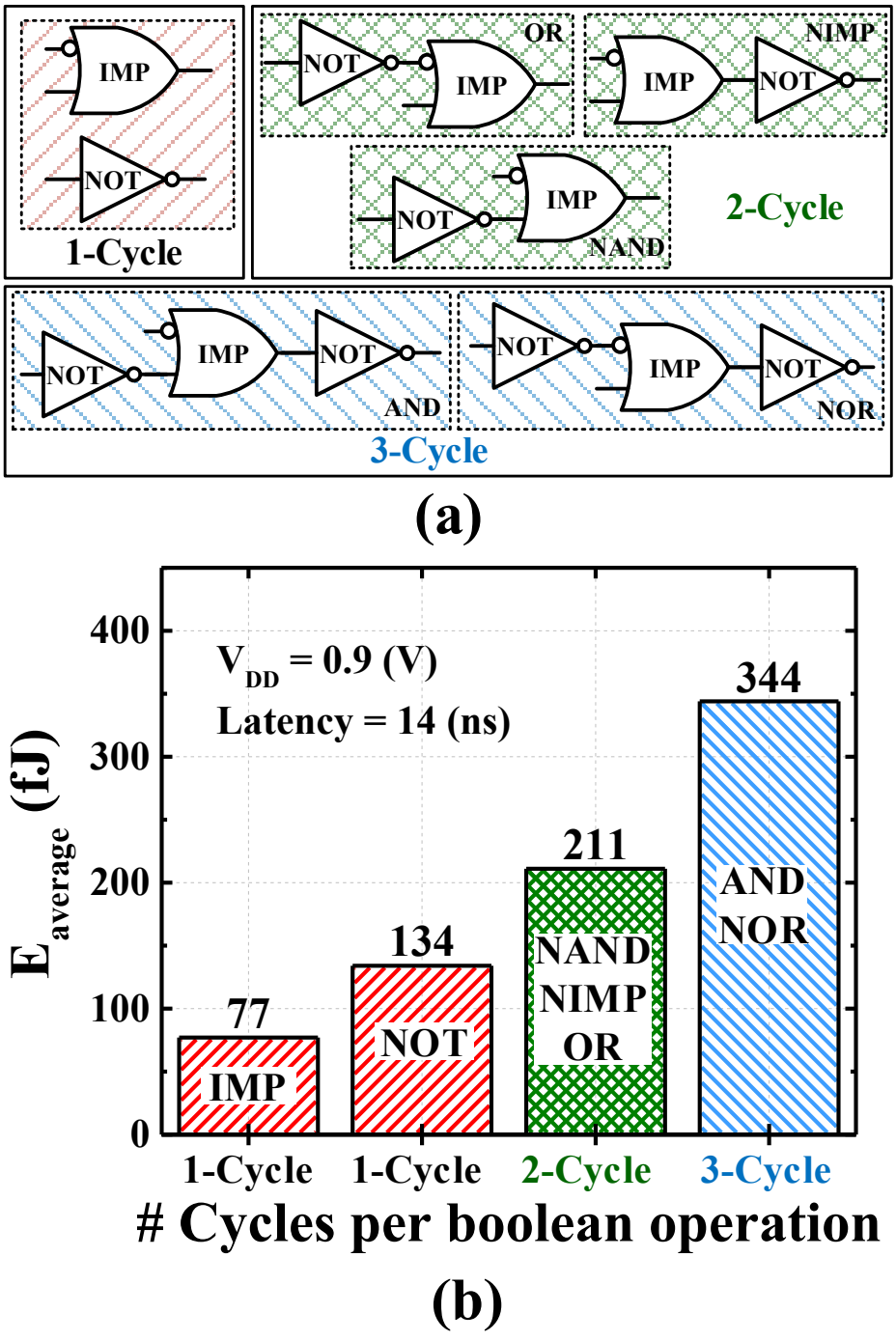

Figure 2.11 (a) Boolean gates based on IMP and NOT operations. (b) Energy consumption comparison of different logic applications.

In contrast to other stateful logic operations reported in literature [59][65], a solution that does not require external magnetic field is provided. In particular in comparison to [59], the proposed approach operates the main logic functions (NOT and IMP) at the same latency, while showing improvement in terms of energy per-bit of about 93% for the IMP operation, while a penalty of about twice the energy consumption for the NOT operation. This is mainly due to the reduced operating voltage and lower latency for the IMP, but a higher one for the NOT. Note that operating at the same latency may ease the design complexity since the system requires a fixed clock frequency.

2.6. Conclusions

The study presented in this chapter was an in-memory logic operation (IMP and NOT) in a system composed by two MTJs and two CMOS access transistors connected in series. The key advantage of this proposal is the achievement of zero field operation by combining VCMA and shape anisotropy, thus making the approach scalable for high integration density. By imposing a proper pulse length for the current, both IMP and NOT logic operations can be performed, without any information about the initial state of the magnetization. The obtained energy/latency results suggest that the approach discussed represents an efficient solution to implement in-memory logic computing. Anyway, it is obvious how the system is not optimized and a better combination of geometry and parameters could increase the stability and the efficiency of the logic gates, as well as the choice of a different MTJ structure, such as double

barrier MTJs [66].

2.7. Acknowledgement

The work has been supported by PETASPIN association (www.petaspin.com).

Chapter 3

3.Magnetic field sensor based on a low-frequency-tail spintronic diode[†]

Spin-torque diodes have shown great potentials and performance in many applicative fields, from microwave detectors to energy harvesters. In this chapter, a study through micromagnetic simulations of a state-of-the-art non-resonant low-frequency-tail spin-torque diode is presented. Simulations are performed at room temperature, and the analysis is done in terms of the DC output voltage as a function of the amplitude of an in-plane external field applied along different directions. It will be shown that there exists a threshold value of the injected AC current amplitude that promotes a linear behavior of the output voltage of field down to the pT range, and such a behavior could be exploited for the design of a magnetic field sensor.

3.1. Introduction

Spin-Torque Diodes (STDs) were born in 2005 [67] with the discovery that a spin-polarized microwave current can be converted into a rectified voltage in magnetic tunnel junctions (MTJs), thanks to a rectification

[†] Adapted from F. Cutugno, L. Mazza, and A. Meo, "Magnetic Field Sensor based on a lowfrequency-tail spintronic diode," Int. J. Appl. Electromagn. Mech. (under review)

phenomenon linked to the ferromagnetic resonance [68]. This effect in MTJs happens when a microwave current is injected with a frequency close to the natural ferromagnetic resonance frequency of one of the electrodes. Here, the current can excite magnetic precession via STT. The magnetoresistance induced oscillations that result from this precession mix with the oscillating current, giving as a output DC voltage component across the tunnel junction[69], [70]. The spin-torque diodes exhibit a number of advantages from their compatibility with the CMOS technology, which allows them to be integrated together in a chip [71], to be the smallest rectifiers developed so far (nanoscale size). STDs can operate in different regimes such as resonant, non-resonant, passive and active. For this reason, they can be used for many applications, ranging from microwave detectors to energy harvesters [72], [73].

Initially, the STD effect was only exploited to measure the spin-transfer torque efficiency in MTJs [74]–[76], but later STDs have shown promising features for the integration in hybrid systems with better performances than the CMOS counterparts, i.e. Schottky diodes [77], [78]. It has been experimentally proved that biased STDs can achieve a sensitivity (defined as the ratio between the rectified output and the input microwave power) larger than 10kV/W, with output resistances smaller than 1 kOhm [77], [79]–[82]. This is possible thanks to the excitation of strongly nonlinear dynamics, such as non-adiabatic stochastic resonance [79], out-of-plane precession [83], nonlinear resonance [80], resonant vortex expulsion [81], as well as injection locking [77]. However, for energy saving in Internet-of-Things nodes and electromagnetic energy harvesting, it is more convenient to design passive detectors that can work

at ultralow power with a large signal-to-noise ratio [83], [84]. The STD effect can be excited by spin-Hall effect [85], [86] and used in probing domain walls dynamics in the free layer and the corresponding domain pattern [87]. It can also be employed in neurocomputing such a spin-torque nano oscillators hardware neural network [88] or sparse neuromorphic computing [89], in sensing, thanks to their very high sensitivity (up to 210 000 mV mW^{-1} [90]), as radiofrequency detectors [83], [91]–[93], passive demodulation of digital signals and microwave imaging [94], [95], as well as in antiferromagnets [96].

A promising application of STDs is the sensing of magnetic field due to the wide and common range of use of these sensors, such as in space [97], navigation and mechanical systems [98], automotive industry [99], industrial automation [100] and biomedicine [101]. The required characteristics of a magnetic sensor are sensitivity, field range, power consumption, costs and linearity [102], [103]. In particular, linearity is crucial for a sensor output as it allows to determine the field intensity univocally, which leads to a simple circuitry, a better error propagation [103] as well as an easier optimization process compared to non-linear sensors [104].

In this chapter, it is shown the use of a non-resonant low-frequency tail STD [40] working in the passive regime as a magnetic field sensor with detectivity down to the range of picotesla. The non-resonancy of the device, in this case, refers to the fact that the injected alternate current is not at the ferromagnetic resonance frequency. This means that the diode can work in a lower frequency regime respect to the typical GHz range of the ferromagnetic resonance. Furthermore, a diode has a low-frequency

tail response when the rectified output increases in magnitude as the frequency decreases[72]. By means of micromagnetic simulations, the effect of an in-plane magnetic field on the rectified output voltage generated by an AC current at the MHz frequencies at room temperature is studied. These results pave the way for a novel application of this type of non-resonant STD.

3.2. Device and Micromagnetic details

In this section, it is presented the simulated device and the behavior of the rectified voltage when varying the in-plane *x* and *y* components of the applied field in the mT range. The simulated elliptical STD is similar to previous studies [105], [106] and its parameters refer to a stack of PtMn(15) /$Co_{70}Fe_{30}$(2.3)/Ru(0.85) / $Co_{40}Fe_{40}B_{20}$(2.4) / MgO(0.8) / $Co_{20}Fe_{60}B_{20}$(1.65) (thickness in nm) as in Figure 3.1.

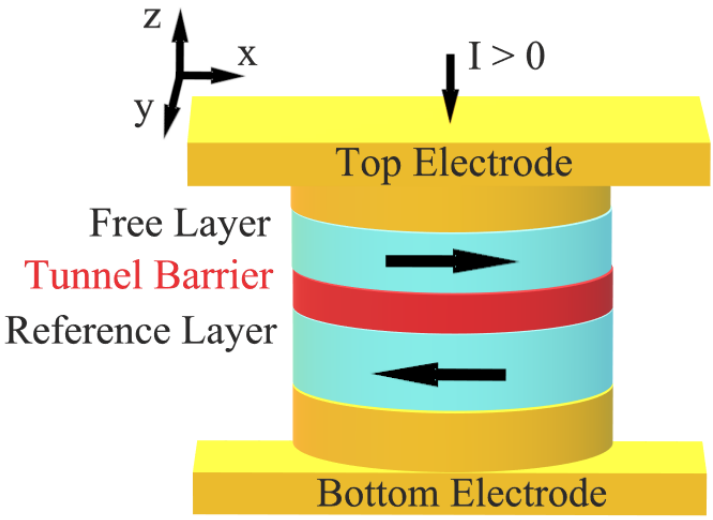

Figure 3.1 Schematics of the STD stack which consists of an in-plane magnetized reference layer and an in-plane magnetized free layer

The dynamics of the magnetization is simulated integrating the LLGS (equation (1.13)), where the saturation magnetization is M_S=950 kA/m, the gyromagnetic ratio is $\mu_0\gamma = 2.21 \times 10^5\ \mathrm{rad} \cdot \frac{\mathrm{m}}{\mathrm{C}}$, and the normalized effective field includes the following contribution: exchange, magnetostatic, anisotropy, external and thermal fields. By recalling the current-torque proportionality coefficient $\sigma = J\sigma_\perp/(1 + \eta^2 \cos\beta)$ for the STT term (equation (1.14)), where the spin-polarization factor is $\eta = 0.66$, $\beta = \arccos(\vec{m} \cdot \vec{m}_p)$ is the angle between the free layer magnetization and pinned layer magnetization $\vec{m}_p$, assumed to be fixed along the x direction ($\vec{m}_p = \hat{x}$, with $\hat{x}$ the x axis unit vector). $\sigma_\perp = (2\eta g\mu_B)/(2\gamma e\, M_s^2 t_{FL})$, where g is the Landé factor, $\mu_B$is the Bohr magneton, e is the electron charge, t_{FL} is the free layer thickness.

The AC current density applied perpendicularly to the elliptic surface of the free layer is $J = J_{AC} \cdot \sin(2\pi ft)$, with a frequency *f* =100 MHz. The geometrical and physical parameters are the same as in a previous work on an analogous system[40]: exchange energy constant *A*=20 pJ/m and and Gilbert damping α=0.02. Here, the uniaxial anisotropy term includes a second order parameter in addition to equation (1.9), and it takes the form:

$$\vec{h}_{an} = \frac{2K_1}{\mu_0 M_s^2}(\vec{m} \cdot \vec{u}_i)\vec{u}_i + \frac{4K_2}{\mu_0 M_s^2}(\vec{m} \cdot \vec{u}_i)^3\vec{u}_i \qquad (3.1)$$

with first order parameter K_1=0.48 MJ/m^3 and second order term K_2=1.5×10^4 J/m^3. The free layer of elliptical section has dimensions of

130×46×1.65 nm^3. The simulations described in the following are performed at room temperature (T=300 K) and the thermal effects are accounted for via the stochastic term (equation (1.12)) $\vec{h}_{th} = \frac{\vec{\chi}}{M_S}\sqrt{\frac{2\alpha_G k_B T}{\mu_0 \gamma_0 \Delta V M_S \Delta t}}$.

3.3. Effect of the in-plane magnetic field

In this section, the behavior of the rectified voltage when varying the in-plane x and y components of the applied field in the mT range is presented.

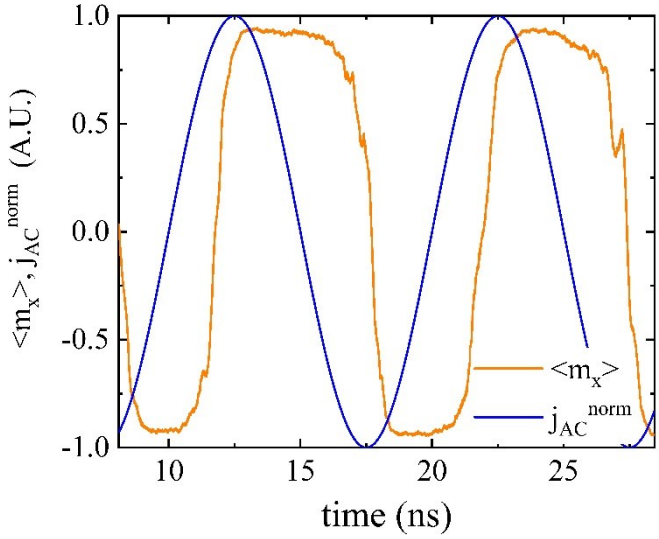

Figure 3.2 Time evolution of the normalized AC current (blue) and the normalized x component of the magnetization (orange) at T = 300 K

First of all, the current density (here J = 2 MA/cm^2 is considered), in the absence of an external field, induces an in-plane precession of the magnetization with the same frequency as the injected current, but with a difference in its phase of about $\Delta\phi$ = 80 degrees, as in Ref. [40], and it is presented in Figure 3.2. The relative time evolution of the dimensionless

resistance calculated as $r = 1 - < m_x > /2$ (with $< m_x >$ being the normalized x component of the magnetization) has the same frequency, but opposite phase to $< m_x >$, as it can be seen in the Figure 3.3.

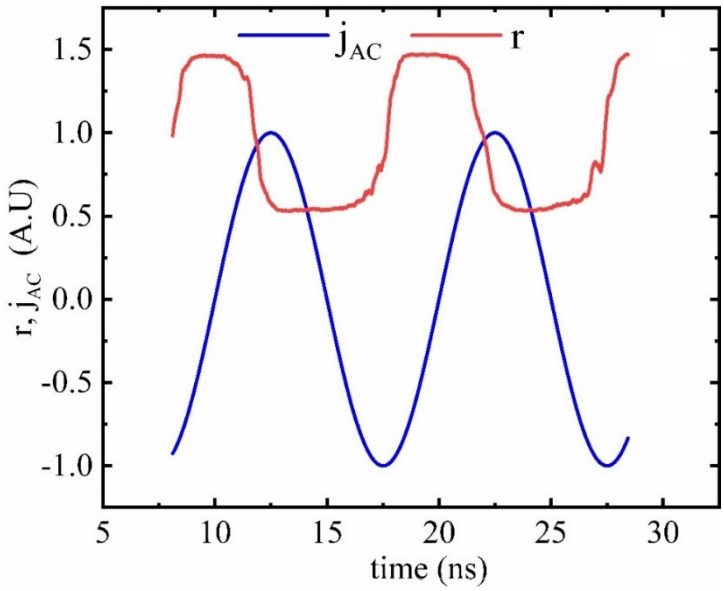

Figure 3.3 Time evolution of the normalized AC current (blue) and the normalized resistance (red)

It is worth noticing that, in this system, the temperature is essential. In fact, temperature aids the current in starting the precession of the magnetization which, otherwise, would need a higher current to drive deterministic jumps between the two minima (magnetization parallel and antiparallel states). This is due to the fact that the temperature gives energy to the system, aiding the jump of the magnetization of the energy barrier between the stable states. The effect of the current on the precession of the x-component of the magnetization in absence of temperature is shown in the following Figure 3.4. Here is showed that the $< m_x >$ cannot reach a wide-angle precession between positive and negative values, but it oscillates weakly around the equilibrium position. By comparing Figure

3.2 with Figure 3.4, it can be seen that with temperature, $< m_x >$ has a complete oscillation, saturating at the maximum value possible. On the other hand, without temperature, the current is not enough to let the system have a wide oscillation, as already said.

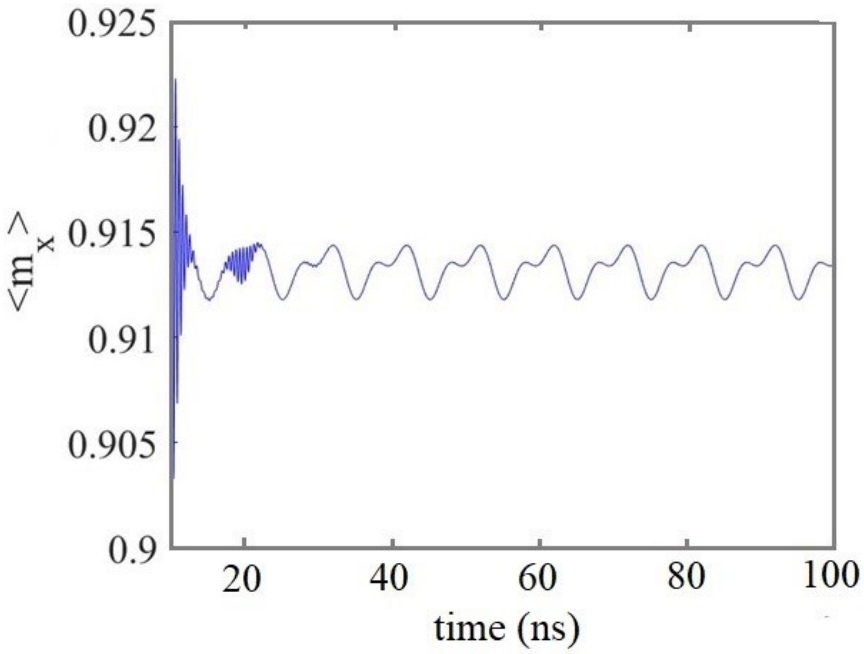

Figure 3.4 Time evolution of the magnetization at T = 0 K without any applied field

Now the effect of applying an in-plane magnetic field on the order of the mT or smaller to this system is considered. Figure 3.5 shows the effect of the external in-plane magnetic field applied along the easy-axis of the free layer *x* direction (Figure 3.5 (a) and (c)), and the *y* direction (Figure 3.5 (b) and (c)), on the rectified voltage V_{DC} and the phase difference $\Delta\phi$. V_{DC} is calculated from:

$$V_{DC} = \langle R(t) \cdot I(t) \rangle = \langle R_S sin(2\pi ft + \phi_1) I_{AC} sin(2\pi ft + \phi_2) \rangle =$$

$$= 0.5 \cdot R_S \cdot I_{AC} \cdot cos(\Delta\phi)$$

(3.2)

where R_s is the amplitude of the oscillating resistance and I_{AC} the amplitude of the electrical current. R_s is estimated directly from the simulations by considering the experimental values of R_{AP}=1660 Ω and R_P=900 Ω [40].

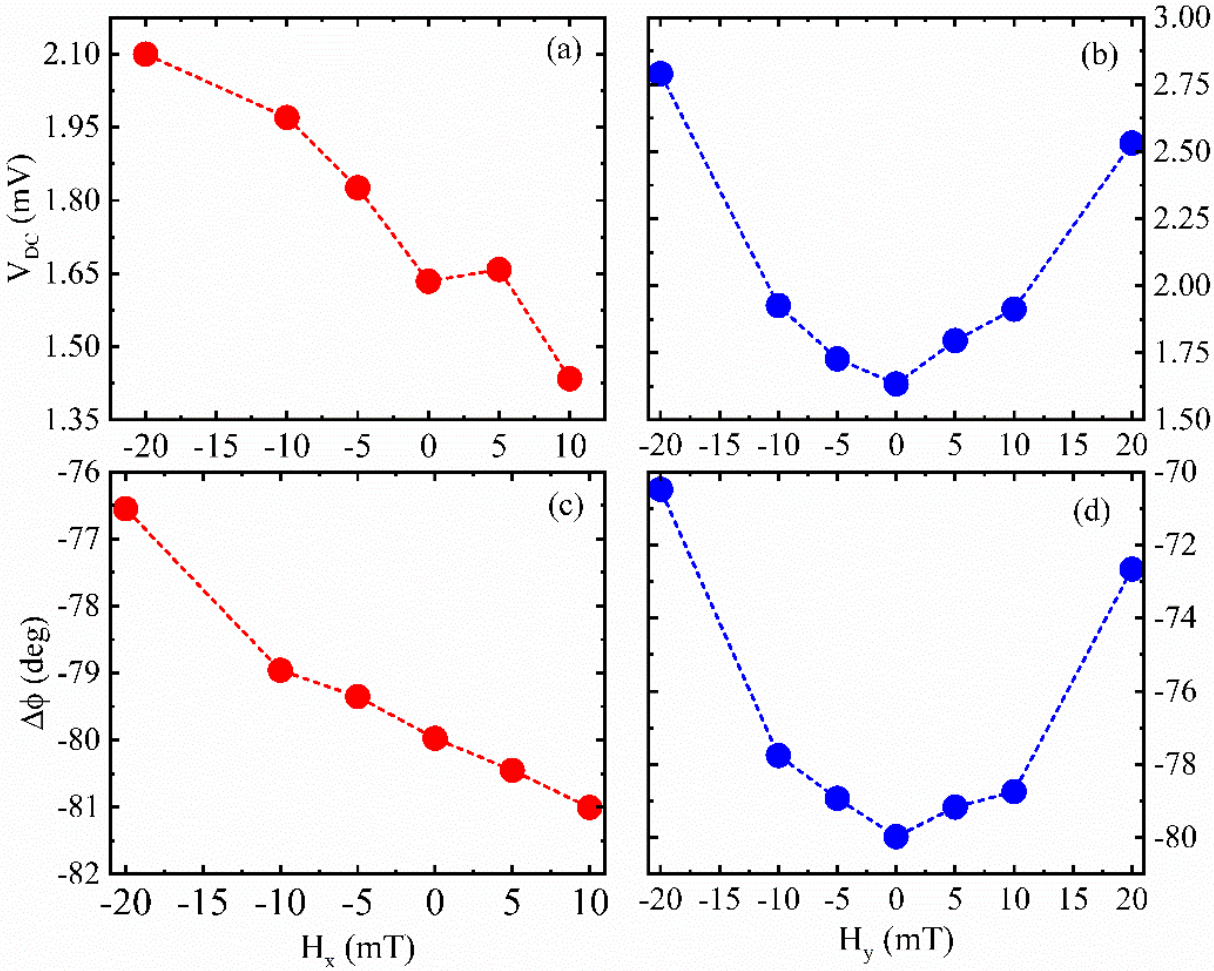

Figure 3.5 Rectified voltage plotted against the applied field along (a) x and (b) y axes, and the phase difference between the magnetization x component and the current density as a function of the applied field along (c) x and (d) y axes

In Figure 3.5 (a) it can be seen that, by applying the external magnetic field along the *x* direction, an almost monotonical behavior of the amplitude of V_{DC} is achieved. Here an increasing of its value for an increasing intensity of the negative *x*-field is shown, along with a decrease for positive *x*-fields. However, there is a small change in the slope around 5 mT, probably due to thermal fluctuations. On the other hand, Figure 3.5 (b) shows that the effect of the field applied along the y direction has an almost symmetric trend for an increasing intensity of the field, both for negative and positive directions, with a minimum at H=0 mT. This difference is given to the fact that the field along y affects the $< m_x >$ precession symmetrically respect to the oscillation axis, while, if applied along x, the external magnetic field assists or opposes oscillations depending on the direction of its application. In fact, the torque due to the external field induces a symmetrical precession if applied along y, instead along x assists or decreases the dynamics induced by the STT.

The behavior of the V_{DC} when the external field is applied along *x* and *y* is accompanied by a similar trend of the phase difference, as shown in panels (c) and (d), respectively, suggesting that the effect of the magnetic field is to induce a change of the phase of the *x* component of the magnetization with the respect to the AC current, without modifying the frequency of the induced magnetization precession.

3.4. Picotesla magnetic field sensor

After characterizing the response over the mT range, the attention on the pT range is now analyzed, by applying a positive field along the free layer

easy-axis. With the aim to use the non-resonant STD as a pT magnetic sensor, what is wanted is a linear response of the rectified voltage on the applied field in this range. To this aim, simulations for fields in the range 8 to 20 pT are performed. The DC voltage exhibits an overall linear behavior, as shown in Figure 3.6 (a). Here, the difference from the ideal linear behavior can be ascribed to the effect of the thermal fluctuations which introduce a random response of the resistance when the effect of the AC current is dominated by the thermal field, and it is likely that the change in slope is also an effect due to the temperature.

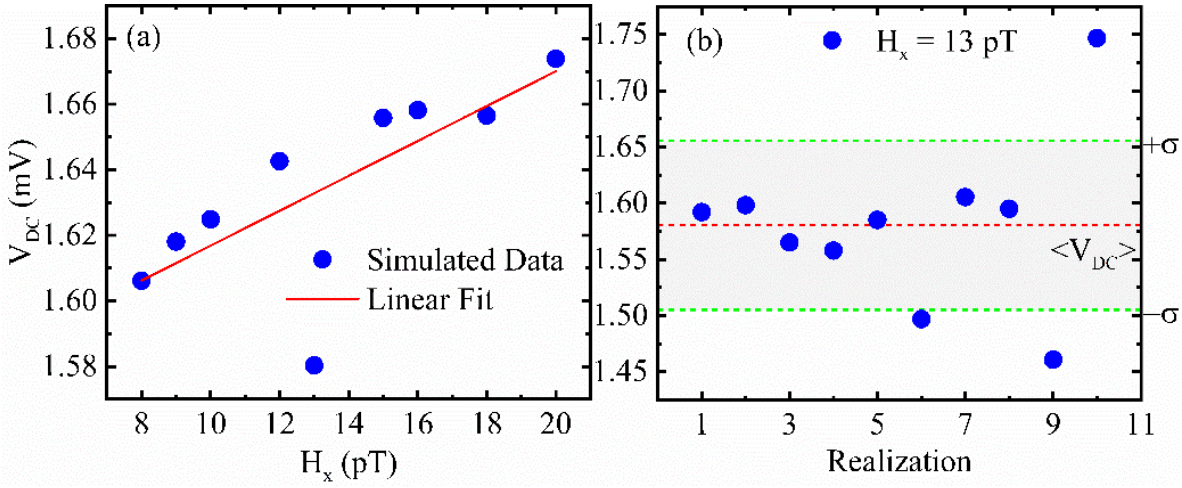

Figure 3.6 a) Rectified voltage (blue dots) for fields applied along the x direction and the linear fit (red straight line) for J_{AC} = 2.0 MA/cm^2 . b) Output voltage for $H_x = 13\ pT$ for various realization number. Red dashed line is the mean, while the green dashed one is the standard deviation. Highlighted gray area is where the data are inside the standard deviation.

To achieve a better understanding of the role of temperature, additional simulations are performed by fixing the in-plane external field to 13 pT for ten different realizations at room temperature (T=300 K). This is done by initializing the gaussian white noise $\vec{\chi}$ in the equation (1.12) with

different seeds, in order to be able to have an idea of statistical fluctuations induced by temperature in the system. The results are shown in Figure 3.6(b), where the output voltages are scattered with the respect to the mean value of the voltage (red dashed line), resulting in a wide standard deviation (green dashed lines). This can suggest the idea that the temperature gives rise to thermal fluctuations so strong that can lead the system to a change of slope from negative to positive, but a better statistic is required to be sure of this hypothesis.

However, it is found that to obtain a linear magnetic field sensor in the pT range, it is enough to calibrate the input AC current. Indeed, by increasing the amplitude of the current density J_{AC} from 2.0 MA/cm^2 to 2.1 MA/cm^2, the V_{DC} behavior as a function of the field exhibits an excellent linear trend. This is shown in Figure 3.7, where the rescaled voltage $\Delta V_{DC} = V_{DC} - V_{DC}(1pT)$ is plotted.

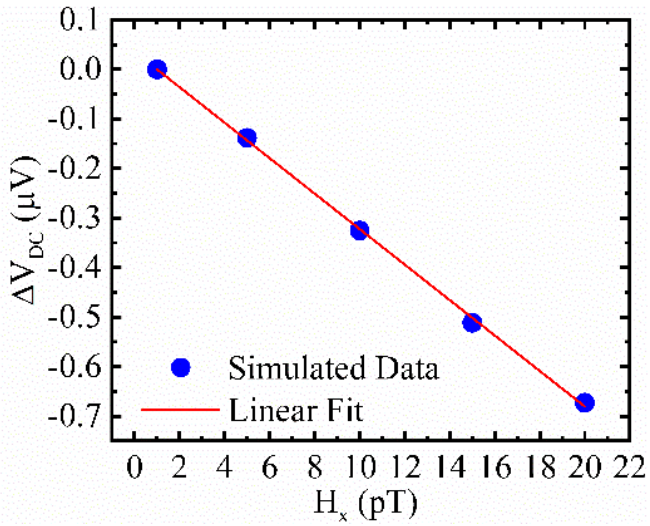

Figure 3.7 Rescaled rectified voltage (blue dots) for fields applied along the x-direction and linear fit (red straight line) of the data for J_{AC}=2.1 MA/cm^2

Moreover, by calculating the voltage difference between 5 pT and 1 pT $\Delta V = V_{DC}(5pT) - V_{DC}(1\ pT) = 0.14\ \mu V$, can be seen that the STD is sensitive to small changes of the external field with a measurable output signal. These results suggest that exists a threshold current that allows to achieve a linear behavior and thus to utilize the STD as a magnetic field sensor at room temperature. This aspect is worth further investigation.

Finally, while it was showed that there exists a threshold current that allows the system to detect effectively a pT magnetic field, it was also found that the slope of $\Delta V(H_{ext})$ has a strong dependence on the intensity of the input current. These last results are presented in Figure 3.8.

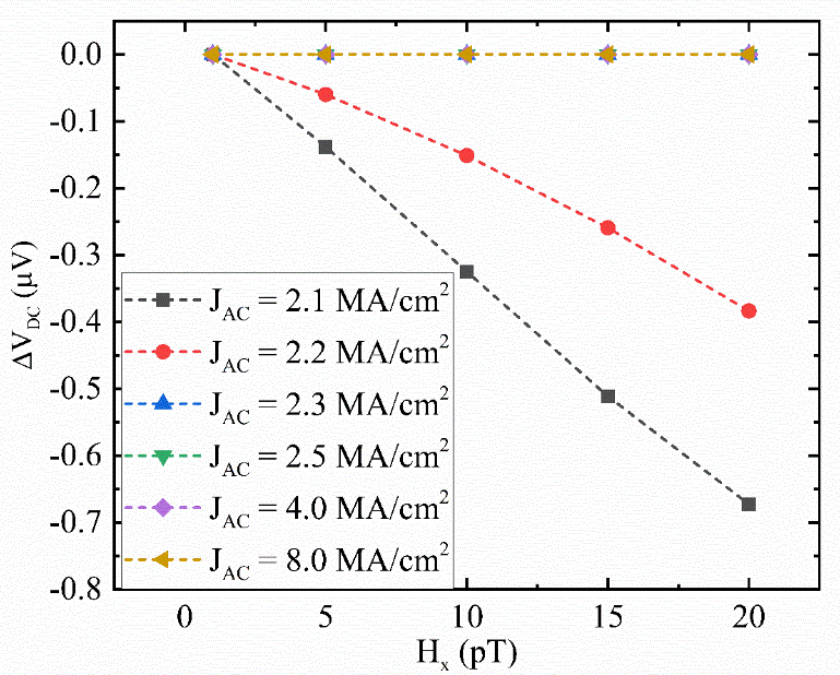

Figure 3.8 Rescaled rectified voltage for increasing current densities.

Here, it can be seen how the slope decreases with stronger currents, becoming practically flat after a few tenths of more current density. This is due to the strong AC current that forces the system in a precise state of oscillation, annihilating any effect of the very small, applied field on the

system. Overall, results shown here prove that is possible to use this system as a sensor for magnetic fields down to the pT by properly tuning the range of AC currents.

3.5. Conclusions

It was shown, by means of micromagnetic simulations, the effect of an in-plane magnetic field applied to a non-resonant low-frequency tail STD excited by an AC current at the MHz frequencies at room temperature. The external field induces changes in the values of the DC output voltage with a monotonical behavior when the in-plane field is applied along the STD easy axis, while the trend is parabolic-like when the field is along the in-plane hard axis. Finally, it was demonstrated that the output voltage as a function of the external field is linear for fields down to the pT range, and that, by tuning the current amplitude above a certain threshold, it is possible the design of a magnetic field sensor based on a non-resonant low-frequency tail STD. Although the results show that this can be achieved only in a reduced range of currents, the early stage of this work opens the door to this new application and to the possibility of optimization.

3.6. Acknowledgement

This work is supported by Project No. PRIN 2020LWPKH7 funded by the Italian Ministry of University and Research, and by the PETASPIN association (www.petaspin.com).

Chapter 4

4.Micromagnetic understanding of switching and self-oscillations in ferrimagnetic materials[‡].

Ferrimagnetic materials represent a promising direction for the realization of spin-based devices, since they can combine the ultrafast dynamics typical of antiferromagnets with an easier way to control the magnetic state typical of ferromagnets. In this chapter, micromagnetic analysis of the magnetization dynamics of a current-driven transition in a ferrimagnet is shown. The system is considered in a spin Hall geometry and the results are expressed as a function of the uncompensation parameter of the angular momentum of the two sublattices. It is found that for a uniaxial FiM, a self-oscillation is the only possible dynamical state at the angular momentum compensation point. Moreover, a finite discontinuity of first kind near the magnetization compensation point is analyzed. The analysis highlights the cause in the demagnetizing field which controls the type of dynamics behind the switching. At the end, the effect of the interfacial Dzyaloshinskii-Moriya interaction will be commented on both switching time and self-oscillations frequency and amplitude.

[‡] Adapted from F. Cutugno, L. Sanchez-Tejerina, R. Tomasello, M. Carpentieri, and G. Finocchio, "Micromagnetic understanding of switching and self-oscillations in ferrimagnetic materials," Appl. Phys. Lett., vol. 118, no. 5, p. 052403, Feb. 2021, doi: 10.1063/5.0038635.

4.1. Introduction

In the last decades, magnetoresistive devices based on ferromagnets have been extensively studied as sensors[108], [109], non-volatile memories[110]–[115], microwave devices, such as detectors and spin-torque nano-oscillators[116]–[119]. However, FMs show some limitations preventing the achievement of larger operational frequencies. An example is the anisotropy-driven precessional dynamics, that limits the operating speeds for microwave devices in the GHz range[114], [120]. Another exemplary problem is the effect of the stray field, which couples neighboring devices and limits the device scalability for memory applications[114], [120]–[122]. A promising solution to overcome these drawbacks involves the use of antiferromagnets. AFMs have no stray fields [122] and their dynamics, governed by the exchange interaction between the sublattices, have a characteristic THz frequency[120]–[123]. Due to the vanishing stray field, AFMs also experience a weaker response to external magnetic fields[124], [125], making them more robust against external perturbations. Despite these known advantages, controlling their states is more complicated. This is because of the material grain structure and the strong influence of the magnetoelastic effects. Furthermore, their net magnetization is zero, so an external magnetic field cannot be used to redefine the state of antiferromagnets[126]–[128].

A promising alternative is represented by ferrimagnetic materials[129], [130]. They ensure THz dynamics as the AFM counterpart, but they allow an easier detection of the magnetic state via well-established optical and electrical methods already applied to FMs, such as the magneto-optical

Kerr effect (MOKE)[131], [132] or anomalous Hall effect (AHE)[133]–[136]. Ferrimagnets can be modeled as AFMs by considering two antiferromagnetically coupled sublattices but, unlike AFMs, the two magnetic sublattices can have a different magnetic moment and angular momentum. Consequently, the net magnetization and angular momentum of FiMs can be varied by changing either their chemical composition[132], [137] or temperature[138], [139]. In FiMs two different interesting compensation points can be found: the magnetic compensation point (MCP), *i.e.* a zero net magnetization state, and an angular momentum compensation point (AMCP), *i.e.* a vanishing net angular momentum compensation state. In the MCP, the system has a net magnetization which is zero, so it's an undesired working point because it is a state difficult to control as for the AFMs. On the other hand, AMCP is the most interesting point, because in the range around it, the dynamic of the FiM is ultrafast AFM-like, but the net magnetization is non zero. These features provide additional ways to tune FiM properties to get the desired characteristics. FiMs have been proposed as memory devices driven by either optical[51], [140]–[142] or electrical switching[130], [135], [143], material-hosting magnetic solitons, such as domain walls and skyrmions for racetrack memories[137], [138], and, recently as nano-oscillators[144]. Although the all-optical switching mechanism exhibits ps switching dynamics[51], [140]–[142], it requires high power to operate. On the other hand, the integration of spintronic systems with conventional electronics requires the electrical manipulation of the magnetization state in low-power devices. For this reason, a focus on the current-driven dynamics in FiMs is done. Up to date, the electrical switching via spin-orbit torques, either

from spin Hall effect [145]–[147] or Rashba effect[148], [149], has been mainly investigated in perpendicular FiMs coupled with a heavy metal (HM) with a large spin-orbit coupling, where an external magnetic field is necessary to achieve a deterministic switching[130], [135], [143]. Moreover, the antisymmetric exchange interaction, that was introduced in the first chapter as interfacial Dzyaloshinskii–Moriya interaction, is expected. This is because this interaction can arise due to the large spin-orbit coupling in the presence of the broken inversion symmetry at the FiM/HM bilayers interface[150]. However, the effect of the IDMI has been treated carefully only in the case of DW motion[138], [151], [152] or skyrmion dynamics[137], [138].

Besides, the theoretical approach used in previous works is based on a macrospin approximation and neglects the demagnetizing field[130], [143], [153]. All these aspects call for a more accurate model to describe the FiM magnetization dynamics and detailed investigations on the role played by the IDMI as well as by the AMCP and MCP to give a deeper insight on the physics behind recent experimental results[154], [155].

In the following sections of this chapter, a systematic study of the SHE-induced switching process and self-oscillations at zero external field in a FiM with an in-plane easy axis is treated. The full micromagnetic framework proposed here goes beyond previous works based on the macrospin approach[130], [143], [144], [153], thus allowing for describing non-uniform magnetization patterns and dynamics, also including the demagnetizing field, which induces non-uniformities and, therefore, plays a role in determining how the switching process occurs. The main discussed results are the divergence of the switching time at the

AMCP and the analysis of a non-monotonic trend with a discontinuity near the MCP. The first result shows that only self-oscillations can be excited as in the case of antiferromagnets[156], [157], while in the second case is shown that the discontinuity is due to the change of the switching mechanism from a uniform to non-uniform one. Moreover, a comparison between the expressions for switching and self-oscillations computed with the macrospin approximation and the micromagnetic simulations is done. This is done in order to prove the validity of this formulas for the estimation of the threshold currents[144] with a more accurate model. Finally, it is shown that the IDMI[30]–[32] has an advantageous effect in promoting shorter switching times, but disadvantageous on the self-oscillations, reducing their amplitude at low applied currents.

4.2. Device and Micromagnetic details

The system considered in the following simulations is a FiM (nominally FeCoGd) device having dimension of $w \times w \times d$, being $w = 100$ nm and $d = 1$ nm, in contact with a heavy metal (HM) (nominally Pt) (see Figure 4.1).

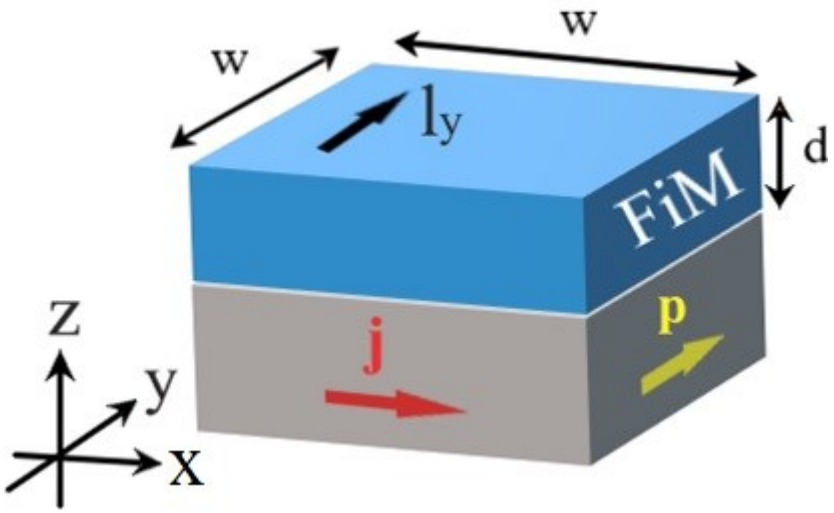

Figure 4.1 A sketch of the geometry of a ferrimagnetic spin Hall device with the indication of Cartesian coordinate system, the current density j and the spin-polarization p directions. The anisotropy easy axis is along the y-direction. The device dimensions are w=100 nm and d=1 nm

The dynamics of the FiM is modeled by two exchange-coupled Landau-Lifshitz-Gilbert (LLG) equations including a Slonczewski-like torque $\tau_{SH,i}$ as in (1.16)

$$\frac{d\vec{m}_i}{dt} = -\gamma_i \vec{m}_i \times \vec{H}_{eff,i} + \alpha \vec{m}_i \times \frac{d\vec{m}_i}{dt} + \tau_{SH,i} \,.$$

where γ_i is the sublattice gyromagnetic ratio ($\gamma_1 = 2.23 \cdot 10^5$ rad·m/C and $\gamma_2 = 2.21 \cdot 10^5$ rad·m/C), computed from the Landé factors[158], α is the Gilbert damping. The exchange interaction is given by three contributions: inhomogeneous intralattice exchange, homogeneous interlattice exchange, and inhomogeneous interlattice exchange, already introduced in section 1.5. Their strengths are characterized by $A_{11} = A_{22}$, A_0, and A_{12}, respectively. The resulting exchange field is the one as in equation (1.17) $H_{exch,i} = \frac{1}{\mu_0 M_{s,i}} \left(2A_{11} \nabla^2 \vec{m}_i + \frac{4A_0}{a^2} \vec{m}_j + A_{12} \nabla^2 \vec{m}_j\right)$,

with a being the lattice constant, μ_0 the vacuum permeability, and $M_{S,i}$ the

i[th] sublattice saturation magnetization. An in-plane uniaxial easy axis along the *y*-direction is considered (Figure 4.1):

$$H_{anis,i} = \frac{2K_u}{\mu_0 M_{s,i}} \left(\vec{m}_i \cdot \vec{u}_y\right)\vec{u}_y \,.$$

where K_u is the uniaxial anisotropy constant.

This choice is done in order to have the Néel vector, defined as $\overrightarrow{l_y} = \overrightarrow{m_i} - \overrightarrow{m_j}$, in an initial state lying on the *y*-axis along either positive or negative direction.

The magnetostatic interaction is computed in the same way as in FM [159]. Another term included is the IDMI[30]–[32] due to the HM underlayer:

$$H_{DMI,i} = -\frac{2D}{\mu_0 M_{s,i}}\left(\vec{u}_z(\nabla \cdot \vec{m}_i) - \nabla \vec{m}_{i,z}\right)$$

where D is the IDMI parameter accounting for the strength of the interaction. The electric current density J flowing into the HM excites SHE-driven dynamics[145]–[147] due to the spin-orbit torque is $\tau_{SH,i} = H_{SH,i}\vec{m}_i \times (\vec{m}_i \times \vec{p})$, with $\vec{p} = \vec{u}_y$ being the direction of the spin current polarization and $H_{SH,i} = \gamma_i(\hbar\theta_{SH}J)/\left(2ed\mu_0 M_{S,i}\right)$ its amplitude. $\hbar$, θ_{SH}, e, and d are the reduced Planck's constant, spin Hall angle, elementary charge, and magnetic layer thickness, respectively.

The change of the angular momenta, corresponding to a variation in temperature or chemical composition in the material, is simulated by varying the saturation magnetization of the second sublattice but keeping constant the gyromagnetic ratios in the angular momentum of the i-th sublattice $S_i = M_{s,i}/\gamma_i$. Therefore, the total angular momentum $S_t = S_1 +$

S_2 differs for negative and positive values.

In this work, the used parameters agree with previous experimental and theoretical works [13], [137], [138], [144]: $A_0 = 0.01$, $A_{11} = A_{22} = 2$ pJ/m, $A_{12} = -2$ pJ/m, $A_0 = -4$ pJ/m, $M_{S1} = 900$ kA/m $K_u = 40$ kJ/m^3, $D = 0.1\ mJ/\mathrm{m}^2$, $d = 1$ nm, $\theta_{SH} = 0.1$, and $a = 0.38$ nm.

4.3. Phase diagram

Figure 4.2 depicts a phase stability diagram of the Néel vector as a function of current density and effective uncompensation factor $\tilde{\nu} = (S_1 - S_2)/(S_1 + S_2)\sqrt{(4A_0)/(a^2|K_u|)}$ [144], as obtained by micromagnetic simulations. This parameter synthetizes the uncompensation between the two sublattices of the ferrimagnet, which could be controlled by changing either the chemical composition [132], [137] or temperature[138], [139] of the FiM, as already told in the introduction of this chapter. Now, the analysis for $\tilde{\nu} > 0$ is presented, where three regions are identified as in the analytical study of Lisenkov *et al.*[144], but also the analysis is extended to negative $\tilde{\nu}$. This choice is dictated by the asymmetry of the threshold current to excite self-oscillations which is due the larger total angular momentum for $\tilde{\nu} < 0$ (see top axis in Figure 4.2). Besides, a large range for the uncompensation parameter is considered to make sure that all the physically relevant scenarios are probed, which can be experimentally realized by tuning the material composition[132], [160].

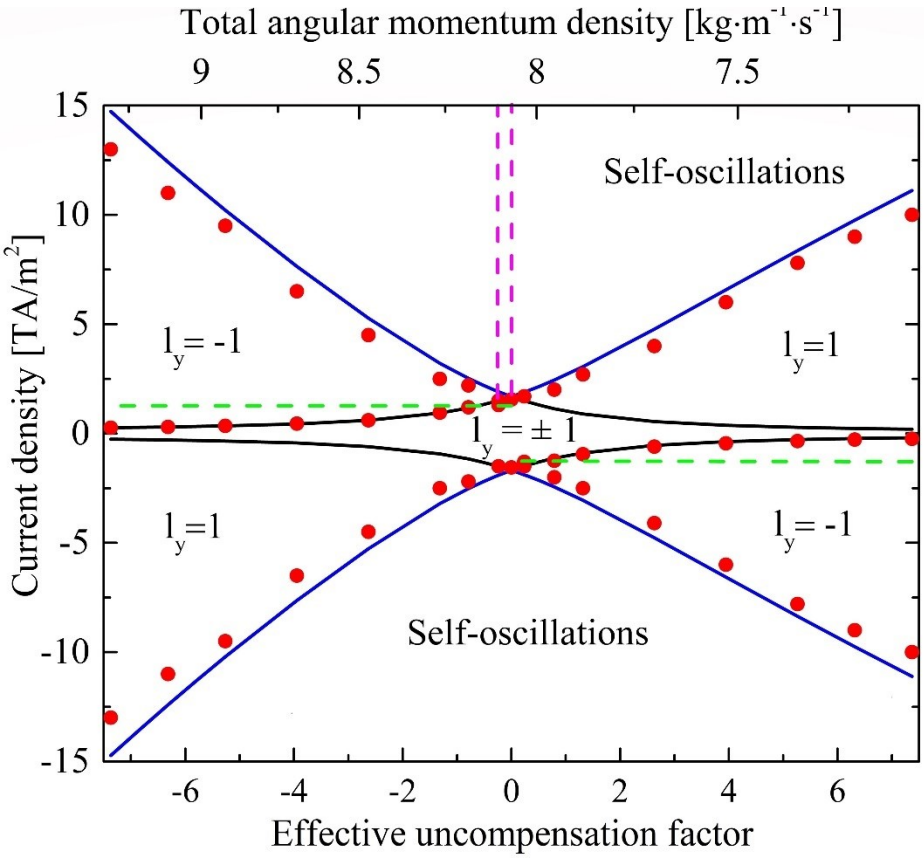

Figure 4.2 Stability phase diagram as a function of the angular momentum uncompensation and the SHE current density obtained with micromagnetic simulations (red dots). The analytical curves computed from equation (7) of Ref. [144] *are also included as solid lines, blue for the transition in the self-oscillation state and black from the identification of the bistable region. The green dashed line indicates the current density* $|j| = 1.3TA/m^2$ *considered for the switching study (see Figure 4.3). The magenta dashed lines indicate the uncompensation parameters values* $\tilde{\nu} = 0$ *and* $\tilde{\nu} = -0.2368$ *considered for the self-oscillations study (see Figure 4.4 and Figure 4.5).*

In the phase diagram presented in Figure 4.2, various areas can be identified. For *J* near zero (region $l_y = \pm 1$ within the black lines), there is bi-stability where the Néel vector remains unperturbed in its initial state, either positive or negative *y*-direction. This region shrinks as $\tilde{\nu}$ increases. When $|J|$ increases, only one state becomes stable, i.e. for positive (negative) *J,* the equilibrium Néel vector is along the positive (negative)

y-direction (regions $l_y = 1\ and\ l_y = -1$). These regions expand as $\tilde{\nu}$ increases and, if the initial state is different from the equilibrium one, the Néel vector undergoes a switching dynamics through a 180º rotation of the two sublattices magnetization. As $|J|$ is further increased, a self-oscillating regime is achieved where the Néel vector makes a precession around the spin accumulation direction, in the case in consideration either y or -y-axis.

4.4. Switching in ferrimagnetic materials

For the particular case of $\tilde{\nu} = 0$ (compensated FiM), the system cannot switch because a limit cycle appears in the energy landscape [144] and the equation (1.16) becomes the same as for the case of antiferromagnets[156], [157]. In fact, from the region $l_y = \pm 1$, by increasing $|J|$, the magnetization goes directly to the self-oscillation dynamics. This micromagnetic results are in agreement with the macrospin threshold currents j_{th} calculated with equation (7) of Ref. [144], so it is still valid in a more accurate analysis. These results are reported in Figure 4.2 as solid blue and solid black lines for clarity. Let's fix the current density to $|J| = 1.3TA/\mathrm{m}^2$ (green dashed line in Figure 4.2) and study the switching dynamics as a function of $\tilde{\nu}$. Figure 4.3(a) shows the switching time computed as the time interval between the application of the current at t=0 ns and the time instant when the normalized y-component of the first sublattice magnetization ($\mathrm{m_{y,1}}$). For $\tilde{\nu} = 0$ (compensated FiM) a permanent self-oscillation dynamics is excited, not shown here. By focusing on negative $\tilde{\nu}$ values, it can be noticed a

discontinuity near the MCP (Figure 4.3 (b)). This abrupt variation is due to a change of the switching mechanism, from uniform switching at $\tilde{\nu} \approx -0.261$ (see Figure 4.3 (c)) to non-uniform switching at $\tilde{\nu} \approx -0.263$ (see Figure 4.3 (d)). The non-uniform process is induced by the demagnetizing field. In fact, by neglecting it, the discontinuity disappears (orange line in Figure 4.3 (b)). More in general, for $\tilde{\nu}$<-0.263, the switching is non-uniform because the demagnetizing field is antiparallel to the Néel vector and has a large enough value, while between $\tilde{\nu}$<-0.263 and MCP the demagnetizing field is still antiparallel but has a negligible modulus. Between the MCP and the AMCP ($-0.24 < \tilde{\nu} < 0$), where the switching is uniform, the demagnetizing field points in the direction of the Néel vector and cannot induce any non-uniformities. For $\tilde{\nu} > 0$, the demagnetizing field is again aligned antiparallel to the Néel vector, and the switching is non-uniform. This effect is compatible with the increasing switching time observed by Cai *et. al.* at the two sides of the MCP[154].

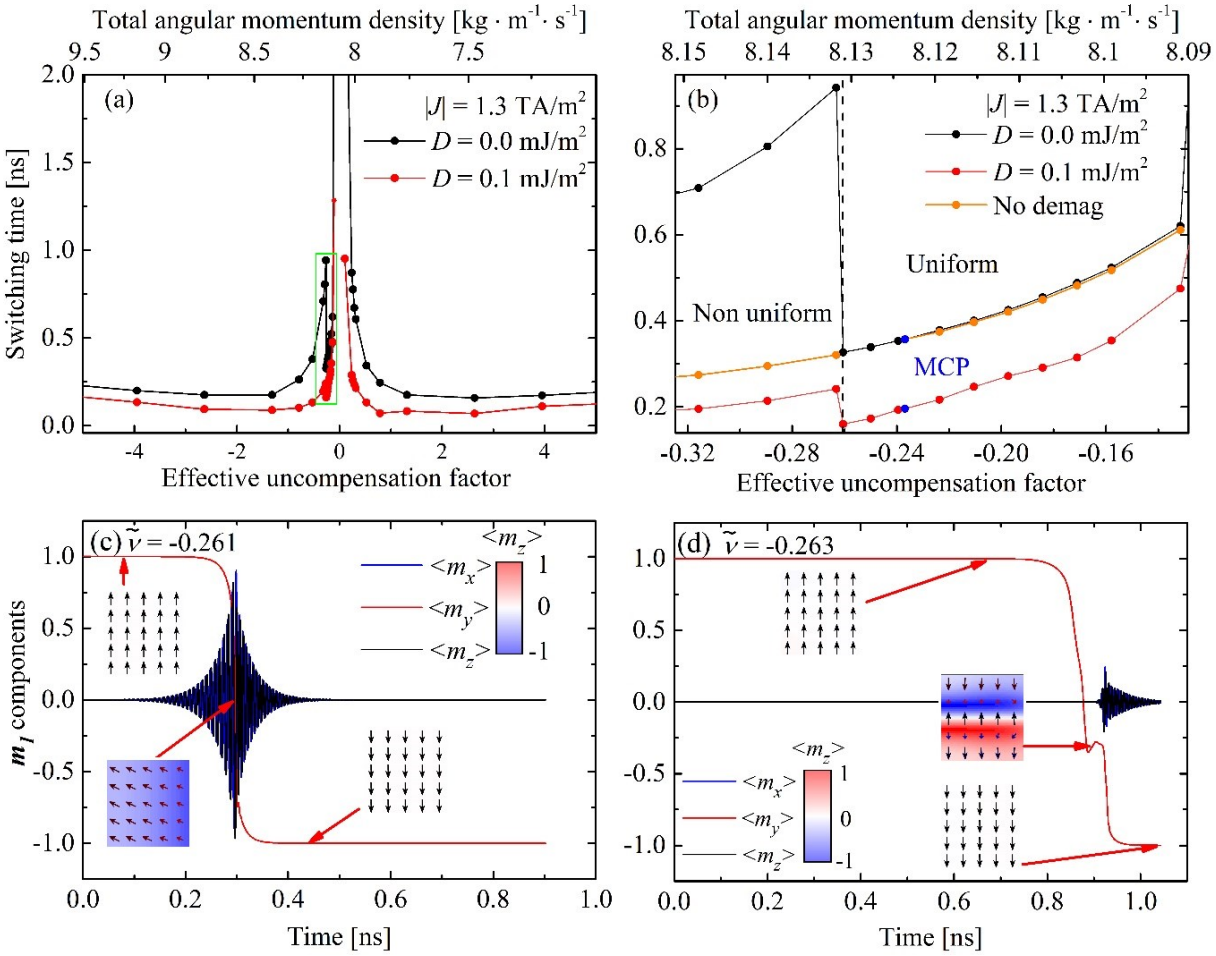

Figure 4.3 Switching time as a function of the effective uncompensation factor of the angular momentum (top axis) of the two sublattices for a current $|J| = 1.3\ TA/m^2$. The black line corresponds to a dynamics without DMI and the red line to a system with non-vanishing DMI. The green rectangle refers to the zoom plotted in (b). (b) Zoom of the region of the magnetization compensation point. Black and red lines keep their correspondence while the orange line stands for simulations without demagnetizing field. (c) Switching of the system at the local minima ($\tilde{\nu} \approx -0.261$). (d) Switching of the system at the local maxima ($\tilde{\nu} \approx -0.263$). The snapshots represent the spatial distribution of the 1st-sublattice magnetization at different time instants, as indicated by the arrows. The colors refer to the z-component of the magnetization.

Furthermore, the effect of the IDMI with $D = 0.1 mJ/m^2$ is considered [138] (red curve in Figure 4.2 (a)). The switching times are smaller than the zero IDMI case for all the $\tilde{\nu}$ range because the IDMI promotes the

nucleation of domains at the sample edges which, eventually, drives the switching. The IDMI also causes the drop of switching time difference at the discontinuity (see Figure 4.3(b) at $\tilde{\nu} \approx -0.262$) since the dynamics are already non-uniform. The results presented here clearly show the IDMI speeds up the switching process by enforcing non-uniform magnetization patterns. Similar qualitative results have been observed in the wide range of current density studied.

4.5. Self-oscillations in ferromagnetic materials

Now, let's fix a value $\tilde{\nu} = 0$ and $\tilde{\nu} = -0.2368$ (AMCP and MCP, respectively, see magenta dashed line in Figure 4.2) and study the self-oscillation frequency and amplitude as a function of the current density. In Figure 4.4, it is showed a linear dependence of the frequency on current that is independent of the IDMI and of compensation point considered, which is in excellent agreement with the macrospin formula from Ref. [144]. This means that the oscillation frequency cannot be affected by the IDMI, so it is independent to the fabrication of the interface, assuming no other changes but the IDMI, as well as by chemical composition or temperature. Thus, it appears that the frequency of the oscillations can be tuned by the only mean of the injected electrical current.

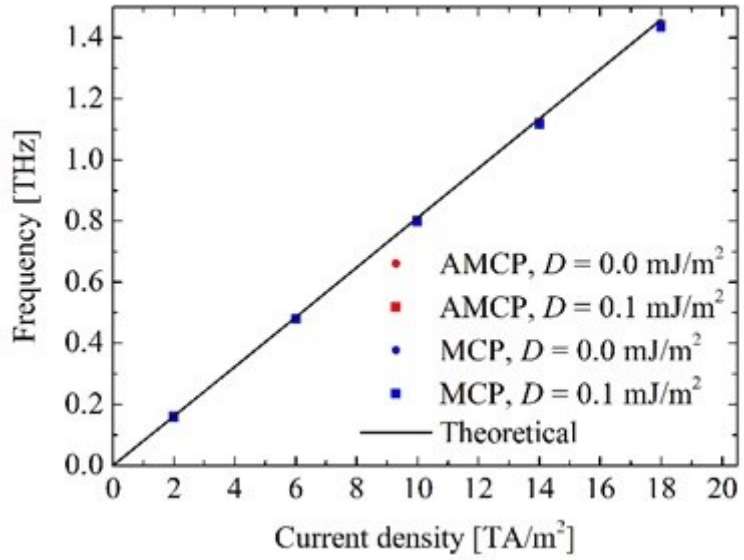

Figure 4.4 Frequency vs applied current. The black line is the macrospin theoretical calculation and points are the results from full micromagnetic simulations at the two compensation points with vanishing and non-vanishing IDMI.

The amplitude of the oscillations non-monotonically decreases as the current increases (Figure 4.5 (a)). This is due to the non-uniform oscillation mediated by domain walls, as shown for $J = 6\,TA/\mathrm{m}^2$ (see Figure 4.5 (b)). For low currents, the domain wall periodicity is larger than the device size and, hence, the whole device oscillates with roughly the same phase (see Figure 4.5 (a) snapshot for $J = 2\,TA/\mathrm{m}^2$). By increasing the current, the periodicity decreases (see Figure 4.5 (a) snapshot for $J = 10\,TA/\mathrm{m}^2$ as well as Figure 4.5 (b)), thus averaging the out-of-plane component of the Néel vector over the sample size and reducing the value of the peak-to-peak amplitude. What can be seen is that there is a minimum of the amplitude, and it is obtained around 10 TA/m^2, when the periodicity is close to the device size. By further increasing the current, the periodicity becomes smaller and the average magnetization value increases (see

magnetization snapshot on Figure 4.5 (a) $J = 14\ TA/\mathrm{m}^2$ where the device size is roughly equal to one and a half period).

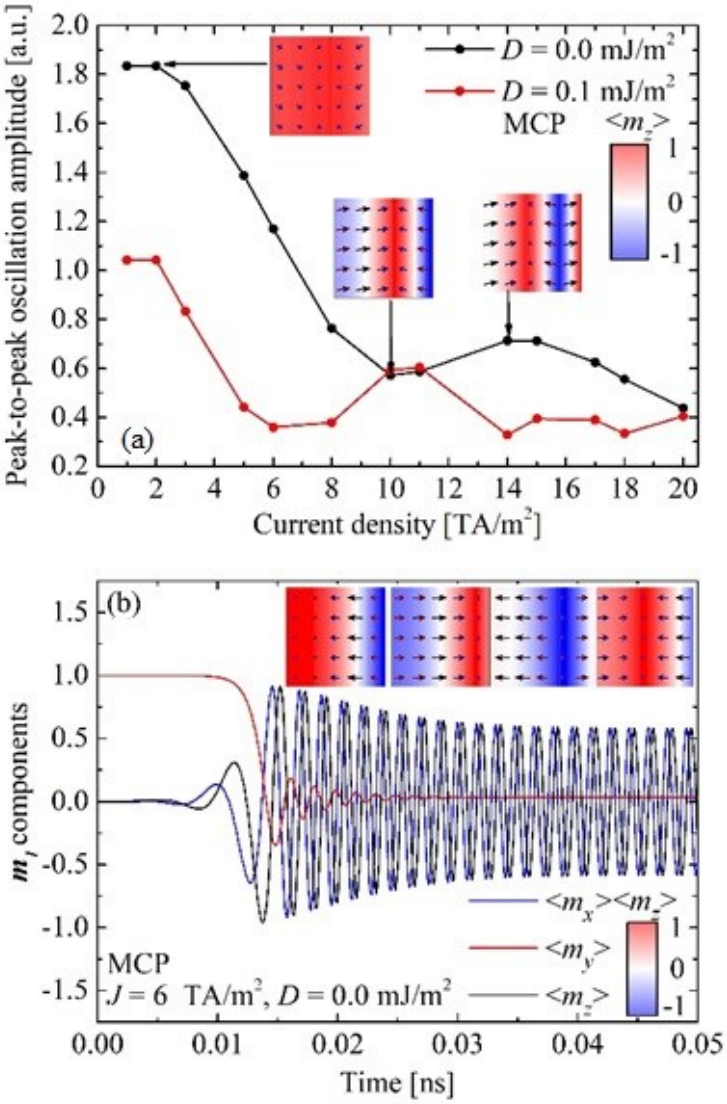

Figure 4.5 (a) Amplitude of self-oscillations at the MCP vs applied current for vanishing and non-vanishing IDMI. (b) Self-oscillating regime at the MCP for a current density of $J = 6\ TA/\mathrm{m}^2$ for a system without IDMI. The snapshots represent the spatial distribution of the 1st-sublattice magnetization at different current densities in (b), as indicated by the arrows, and different times. The colors refer to the z-component of the magnetization.

The presence of the IDMI does not affect either the threshold current or the output frequency. However, it promotes non-uniform oscillations thus

further reducing the non-uniform periodicity. Consequently, for non-zero IDMI the peak-to-peak amplitude decreases more rapidly by keeping the same qualitative trend shifted to smaller currents and its values are in general smaller. Because the output signal depends on the amplitude of self-oscillations, the effect of the IDMI is detrimental if the FiM is used as THz source, in particular, in the range of intermediate currents (below 5 TA/m^2). As a final remark, the existence of a non-uniform magnetization configuration requires the use of full micromagnetic simulations to compute the power signal which is a crucial parameter to determine the viability of a real THz device.

4.6. Conclusions

In this chapter a study on the magnetization dynamics in a FiM/HM bilayer by full micromagnetic simulations is presented, which includes the demagnetizing and IDMI fields. This approach allows to capture the crucial effect of non-uniform dynamics on the system dynamics, something that cannot be caught by the macrospin approximation. It is reported the switching time as a function of the uncompensation parameter for a given current. In particular, it is shown how the switching time diverges at the AMCP while the only solution is a self-oscillation, and more interestingly, a finite discontinuity of the switching time near the MCP. The reason is that at the two sides of this point, the demagnetizing field changes the direction with respect to the Néel vector orientation. Therefore, the switching mechanism changes from uniform to non-uniform with a corresponding increase of the switching time. Furthermore,

it was pointed out how threshold currents and frequency of self-oscillations are well described by the analytical macrospin formula. Additionally, it was analyzed the effect of the IDMI on the design of magnetic memories and spin torque nano-oscillators. This is beneficial for the use of FiMs as storage devices, since it promotes shorter switching times as it advantageously assists the non-homogeneous switching mechanism. On the other hand, it is detrimental for the applicability of FiM as THz sources because it induces a significant reduction of the self-oscillations amplitude at low currents. These results give a better insight on the dynamics excited in FiMs. Thus, this work provides a background for the design of more performant ferrimagnetic memory and THz nano-oscillator devices.

4.7. Acknowledgement

This work was developed with contribution of the COST Action CA17123 “Ultrafast optomagneto-electronics for nondissipative information technology” and the Grant No. 2019-1-U.0. (“Diodi spintronici rad-hard ad elevata sensitività - DIOSPIN”) funded by the Italian Space Agency (ASI) within the call “Nuove idee per la componentistica spaziale del futuro”. This work was also partially supported by the PETASPIN association.

Chapter 5

5.Conclusions

This dissertation deals with the many potential technological applications of spintronics devices. In particular, two applications of MTJ are proposed, a logic gate and a magnetic field sensor, along with a study of the magnetization dynamics of ferrimagnetic materials, to favor possible future exploitations of these materials. The tool that has been used for this work is the micromagnetic approach. This kind of simulations yields an accurate quantitative study of the treated systems, allowing to study and propose new possible devices. Furthermore, it aids in the achievement of a better understanding of properties that are the result of an intricate game of equilibria between different energetic contributions.

The first chapter is a concise introduction to the topic itself, focusing on the models needed for develop the study presented in this thesis, and explaining the used tools, that should help in understanding properly the following chapters.

The second chapter presents the results obtained on in-memory logic operations (IMP and NOT). The system, composed by two MTJs and two CMOS access transistors connected in series, possesses the key advantage of achieving a field-free operation, obtained by the combination of VCMA and shape anisotropy, thus making the approach scalable for high integration density. A study on the dependence on a proper current pulse length for both IMP and NOT logic operations is presented. It highlights

that these operations can be performed without any information about the initial state of the magnetization, simplifying the way of performing the derived logic operations. The obtained energy/latency results suggest that the approach represents an efficient solution to implement in-memory logic computing. This opens to the possibility of actual application of these solutions, subsequent to a rigorous optimization of the device.

In chapter 3, the effect of an in-plane magnetic field applied to a non-resonant low-frequency tail STD excited by an AC current at the MHz frequencies at room temperature on the DC output voltage is presented. The external field induces changes in the DC voltage output of the STD. In particular, is pointed out how in the mT range, the voltage has a linear behavior when the in-plane field is applied along the STD easy axis. Instead, the trend results to be parabolic-like when the field is along the in-plane hard axis. Finally, going down to the pT range, it is shown that the output voltage is linear with the external field, and that, by tuning the current amplitude above a certain threshold, it is possible to design a magnetic field sensor based on this technology. The results presented here represent an initial study on the topic, hence a deeper comprehension of this effect is needed in order to develop an efficient sensor.

In chapter 4, a full micromagnetic study on the magnetization dynamics in a FiM/HM bilayer is presented. This analysis includes the demagnetizing and IDMI fields contribution to the behavior of the system. The important effect of non-uniform magnetization dynamics on the system properties, something that cannot be caught by the macrospin approximation, is shown. It is shown the switching time as function of the uncompensation parameter diverges at the AMCP while the only solution

is a self-oscillation, and there is a finite discontinuity of the switching time near the MCP. The reason is that at the two sides of this point, the demagnetizing field changes the direction with respect to the Néel vector orientation. Therefore, the switching mechanism changes from uniform to non-uniform with a corresponding increase of the switching time. It is also shown that threshold currents and frequency of self-oscillations are well described by the analytical macrospin formula. Additionally, the effect of the IDMI is analyzed, in order to understand how it could impact the design of magnetic memories and spin torque nano-oscillators. It is beneficial for the use of FiMs as storage devices since it promotes shorter switching times as it advantageously assists the non-homogeneous switching mechanism. On the contrary, it is detrimental for the applicability of FiM as THz sources because it induces a significant reduction of the self-oscillations' amplitude at low currents. These results give a better insight on the dynamics excited in FiMs, proving useful in the design of more performant ferrimagnetic memory and THz nano-oscillator devices.

Bibliography

[1] R. Meservey, P. M. Tedrow, and P. Fulde, “Magnetic Field Splitting of the Quasiparticle States in Superconducting Aluminum Films,” *Phys. Rev. Lett.*, vol. 25, no. 18, pp. 1270–1272, Nov. 1970, doi: 10.1103/PhysRevLett.25.1270.

[2] M. Julliere, “Tunneling between ferromagnetic films,” *Phys. Lett. A*, vol. 54, no. 3, pp. 225–226, Sep. 1975, doi: 10.1016/0375-9601(75)90174-7.

[3] M. Johnson and R. H. Silsbee, “Interfacial charge-spin coupling: Injection and detection of spin magnetization in metals,” *Phys. Rev. Lett.*, vol. 55, no. 17, pp. 1790–1793, Oct. 1985, doi: 10.1103/PhysRevLett.55.1790.

[4] M. N. Baibich *et al.*, “Giant Magnetoresistance of (001)Fe/(001)Cr Magnetic Superlattices,” *Phys. Rev. Lett.*, vol. 61, no. 21, pp. 2472–2475, Nov. 1988, doi: 10.1103/PhysRevLett.61.2472.

[5] G. Binasch, P. Grünberg, F. Saurenbach, and W. Zinn, “Enhanced magnetoresistance in layered magnetic structures with antiferromagnetic interlayer exchange,” *Phys. Rev. B*, vol. 39, no. 7, pp. 4828–4830, Mar. 1989, doi: 10.1103/PhysRevB.39.4828.

[6] L. D. Landau and E. M. Lifshitz, “ON THE THEORY OF THE DISPERSION OF MAGNETIC PERMEABILITY IN FERROMAGNETIC BODIES,” 1935.

[7] W. F. Brown, *Micromagnetics*. J. Wiley, 1963.

[8] E. H. Frei, S. Shtrikman, and D. Treves, “Critical Size and Nucleation Field of Ideal Ferromagnetic Particles,” *Phys. Rev.*, vol.

106, no. 3, pp. 446–455, May 1957, doi: 10.1103/PhysRev.106.446.

[9] R. Verba *et al.*, “Correction of Phase Errors in a Spin-Wave Transmission Line by Nonadiabatic Parametric Pumping,” *Phys. Rev. Appl.*, vol. 11, no. 5, p. 054040, May 2019, doi: 10.1103/PhysRevApplied.11.054040.

[10] R. Li *et al.*, “A spin–orbit torque device for sensing three-dimensional magnetic fields,” *Nat. Electron.*, vol. 4, no. 3, pp. 179–184, Feb. 2021, doi: 10.1038/s41928-021-00542-8.

[11] B. Fang *et al.*, “Giant spin-torque diode sensitivity in the absence of bias magnetic field,” *Nat. Commun.*, vol. 7, 2016, doi: 10.1038/ncomms11259.

[12] A. Giordano, G. Finocchio, L. Torres, M. Carpentieri, and B. Azzerboni, “Semi-implicit integration scheme for Landau–Lifshitz–Gilbert-Slonczewski equation,” *J. Appl. Phys.*, vol. 111, no. 7, p. 07D112, 2012, doi: 10.1063/1.3673428.

[13] L. Sánchez-Tejerina, R. Tomasello, V. Puliafito, B. Azzerboni, M. Carpentieri, and G. Finocchio, “Unified Framework for Micromagnetic Modeling of Ferro-, Ferri-, and Antiferromagnetic Materials at Mesoscopic Scale: Domain Wall Dynamics as a Case Study,” *IEEE Magn. Lett.*, vol. 11, pp. 1–5, 2020, doi: 10.1109/LMAG.2020.3022602.

[14] K. Ramstock, A. Hubert, and D. Berkov, “Techniques for the computation of embedded micromagnetic structures,” *IEEE Trans. Magn.*, vol. 32, no. 5, pp. 4228–4230, 1996, doi: 10.1109/20.539342.

[15] J. Fidler and T. Schrefl, “Micromagnetic modelling - the current

state of the art," *J. Phys. D. Appl. Phys.*, vol. 33, no. 15, pp. R135–R156, Aug. 2000, doi: 10.1088/0022-3727/33/15/201.

[16] R. Rosenberg, "Magnetostatic principles in ferromagnetism, vol. 1: W.F. Brown: Selected topics in solid state physics, North Holland Publishing Co., Amsterdam 1962. pp. 202 \$7.75," *Solid. State. Electron.*, vol. 7, pp. 938–939, 1964.

[17] M. d'Aquino, "Nonlinear Magnetization Dynamics in Thin-Films and Nanoparticles," 2005.

[18] T. L. Gilbert, "Classics in Magnetics A Phenomenological Theory of Damping in Ferromagnetic Materials," *IEEE Trans. Magn.*, vol. 40, no. 6, pp. 3443–3449, Nov. 2004, doi: 10.1109/TMAG.2004.836740.

[19] T. L. Gilbert, "A Lagrangian Formulation of the Gyromagnetic Equation of the Magnetization Field," *Phys. Rev. D*, vol. 100, p. 1243, 1955.

[20] G. Bertotti, "Hysteresis in Magnetism: For Physicists, Materials Scientists, and Engineers," 1998.

[21] S. Blundell 1967-, *Magnetism in condensed matter*. Oxford ; New York : Oxford University Press, 2001., 2001.

[22] N. W. Ashcroft, "Solid state physics [by] Neil W. Ashcroft [and] N. David Mermin.," 1976.

[23] M. T. Johnson, P. J. H. Bloemen, F. J. A. den Broeder, and J. J. de Vries, "Magnetic anisotropy in metallic multilayers," *Reports Prog. Phys.*, vol. 59, no. 11, pp. 1409–1458, Nov. 1996, doi: 10.1088/0034-4885/59/11/002.

[24] T. Nozaki *et al.*, "Recent Progress in the Voltage-Controlled

Magnetic Anisotropy Effect and the Challenges Faced in Developing Voltage-Torque MRAM," *Micromachines* , vol. 10, no. 5. 2019, doi: 10.3390/mi10050327.

[25] J. Zhu *et al.*, "Voltage-Induced Ferromagnetic Resonance in Magnetic Tunnel Junctions," *Phys. Rev. Lett.*, vol. 108, no. 19, p. 197203, May 2012, doi: 10.1103/PhysRevLett.108.197203.

[26] W. G. Wang, M. Li, S. Hageman, and C. L. Chien, "Electric-field-assisted switching in magnetic tunneljunctions," *Nat. Mater.*, vol. 11, no. 1, pp. 64–68, 2012, doi: 10.1038/nmat3171.

[27] R. De Rose *et al.*, "A Compact Model with Spin-Polarization Asymmetry for Nanoscaled Perpendicular MTJs," *IEEE Trans. Electron Devices*, vol. 64, no. 10, pp. 4346–4353, Oct. 2017, doi: 10.1109/TED.2017.2734967.

[28] N. Perez, L. Torres, and E. Martinez-Vecino, "Micromagnetic Modeling of Dzyaloshinskii–Moriya Interaction in Spin Hall Effect Switching," *IEEE Trans. Magn.*, vol. 50, no. 11, pp. 1–4, Nov. 2014, doi: 10.1109/TMAG.2014.2323707.

[29] M. Bode *et al.*, "Chiral magnetic order at surfaces driven by inversion asymmetry," *Nature*, vol. 447, no. 7141, pp. 190–193, May 2007, doi: 10.1038/nature05802.

[30] D. Cortés-Ortuño *et al.*, "Proposal for a micromagnetic standard problem for materials with Dzyaloshinskii{\textendash}Moriya interaction," *New J. Phys.*, vol. 20, no. 11, p. 113015, Nov. 2018, doi: 10.1088/1367-2630/aaea1c.

[31] A. Thiaville, S. Rohart, É. Jué, V. Cros, and A. Fert, "Dynamics of Dzyaloshinskii domain walls in ultrathin magnetic films," *EPL*

(Europhysics Lett., vol. 100, no. 5, p. 57002, 2012, doi: 10.1209/0295-5075/100/57002.

[32] N. Perez, L. Torres, and E. Martinez-Vecino, “Micromagnetic Modeling of Dzyaloshinskii-Moriya Interaction in Spin Hall Effect Switching,” *IEEE Trans. Magn.*, vol. 50, no. 11, pp. 1–4, 2014, doi: 10.1109/TMAG.2014.2323707.

[33] W. F. Brown, “Thermal Fluctuations of a Single-Domain Particle,” *Phys. Rev.*, vol. 130, no. 5, pp. 1677–1686, Jun. 1963, doi: 10.1103/PhysRev.130.1677.

[34] G. Finocchio, I. N. Krivorotov, X. Cheng, L. Torres, and B. Azzerboni, “Micromagnetic understanding of stochastic resonance driven by spin-transfer-torque,” *Phys. Rev. B*, vol. 83, no. 13, p. 134402, 2011, doi: 10.1103/PhysRevB.83.134402.

[35] J. C. Slonczewski, “Current-driven excitation of magnetic multilayers,” *J. Magn. Magn. Mater.*, vol. 159, no. 1–2, pp. L1–L7, Jun. 1996, doi: 10.1016/0304-8853(96)00062-5.

[36] L. Berger, “Emission of spin waves by a magnetic multilayer traversed by a current,” *Phys. Rev. B - Condens. Matter Mater. Phys.*, vol. 54, no. 13, pp. 9353–9358, 1996, doi: 10.1103/PhysRevB.54.9353.

[37] M. Madami *et al.*, “Direct observation of a propagating spin wave induced by spin-transfer torque,” *Nat. Nanotechnol.*, vol. 6, no. 10, pp. 635–638, Oct. 2011, doi: 10.1038/nnano.2011.140.

[38] V. E. Demidov, S. Urazhdin, and S. O. Demokritov, “Direct observation and mapping of spin waves emitted by spin-torque nano-oscillators,” *Nat. Mater.*, vol. 9, no. 12, pp. 984–988, Dec.

2010, doi: 10.1038/nmat2882.

[39] G. Finocchio *et al.*, “Perspectives on spintronic diodes,” *Appl. Phys. Lett.*, vol. 118, no. 16, 2021, doi: 10.1063/5.0048947.

[40] R. Tomasello *et al.*, “Low-Frequency Nonresonant Rectification in Spin Diodes,” *Phys. Rev. Appl.*, vol. 14, no. 2, p. 024043, Aug. 2020, doi: 10.1103/PhysRevApplied.14.024043.

[41] V. M. Edelstein, “Spin polarization of conduction electrons induced by electric current in two-dimensional asymmetric electron systems,” *Solid State Commun.*, vol. 73, no. 3, pp. 233–235, Jan. 1990, doi: 10.1016/0038-1098(90)90963-C.

[42] A. Manchon, H. C. Koo, J. Nitta, S. M. Frolov, and R. A. Duine, “New perspectives for Rashba spin–orbit coupling,” *Nat. Mater.*, vol. 14, no. 9, pp. 871–882, Sep. 2015, doi: 10.1038/nmat4360.

[43] H. Kontani, T. Tanaka, D. S. Hirashima, K. Yamada, and J. Inoue, “Giant Orbital Hall Effect in Transition Metals: Origin of Large Spin and Anomalous Hall Effects,” *Phys. Rev. Lett.*, vol. 102, no. 1, p. 016601, Jan. 2009, doi: 10.1103/PhysRevLett.102.016601.

[44] D. Jo, D. Go, and H.-W. Lee, “Gigantic intrinsic orbital Hall effects in weakly spin-orbit coupled metals,” *Phys. Rev. B*, vol. 98, no. 21, p. 214405, Dec. 2018, doi: 10.1103/PhysRevB.98.214405.

[45] F. Freimuth, S. Blügel, and Y. Mokrousov, “The inverse thermal spin–orbit torque and the relation of the Dzyaloshinskii–Moriya interaction to ground-state energy currents,” *J. Phys. Condens. Matter*, vol. 28, no. 31, p. 316001, Aug. 2016, doi: 10.1088/0953-8984/28/31/316001.

[46] T. Kimura, Y. Otani, T. Sato, S. Takahashi, and S. Maekawa,

"Room-Temperature Reversible Spin Hall Effect," *Phys. Rev. Lett.*, vol. 98, no. 15, p. 156601, Apr. 2007, doi: 10.1103/PhysRevLett.98.156601.

[47] S. O. Valenzuela and M. Tinkham, "Direct electronic measurement of the spin Hall effect," *Nature*, vol. 442, no. 7099, pp. 176–179, Jul. 2006, doi: 10.1038/nature04937.

[48] M. ~I. D'Yakonov and V. ~I. Perel', "Possibility of Orienting Electron Spins with Current," *Sov. J. Exp. Theor. Phys. Lett.*, vol. 13, p. 467, 1971.

[49] Y. Wang, P. Deorani, X. Qiu, J. H. Kwon, and H. Yang, "Determination of intrinsic spin Hall angle in Pt," *Appl. Phys. Lett.*, vol. 105, no. 15, p. 152412, Oct. 2014, doi: 10.1063/1.4898593.

[50] L. Sánchez-Tejerina, V. Puliafito, P. Khalili Amiri, M. Carpentieri, and G. Finocchio, "Dynamics of domain-wall motion driven by spin-orbit torque in antiferromagnets," *Phys. Rev. B*, vol. 101, no. 1, p. 14433, Jan. 2020, doi: 10.1103/PhysRevB.101.014433.

[51] C. D. Stanciu *et al.*, "All-Optical Magnetic Recording with Circularly Polarized Light," *Phys. Rev. Lett.*, vol. 99, no. 4, p. 47601, Jul. 2007, doi: 10.1103/PhysRevLett.99.047601.

[52] S. Jain, S. Sapatnekar, J.-P. Wang, K. Roy, and A. Raghunathan, "Computing-in-memory with spintronics," in *2018 Design, Automation & Test in Europe Conference & Exhibition (DATE)*, Mar. 2018, pp. 1640–1645, doi: 10.23919/DATE.2018.8342277.

[53] A. Lyle, J. Harms, S. Patil, X. Yao, D. J. Lilja, and J.-P. Wang, "Direct communication between magnetic tunnel junctions for nonvolatile logic fan-out architecture," *Appl. Phys. Lett.*, vol. 97,

no. 15, p. 152504, Oct. 2010, doi: 10.1063/1.3499427.

[54] M. Horowitz, “1.1 Computing’s energy problem (and what we can do about it),” in *2014 IEEE International Solid-State Circuits Conference Digest of Technical Papers (ISSCC)*, Feb. 2014, pp. 10–14, doi: 10.1109/ISSCC.2014.6757323.

[55] H. Mahmoudi, T. Windbacher, V. Sverdlov, and S. Selberherr, “Stateful STT-MRAM-Based Logic for Beyond–Von Neumann Computing,” in *Micro- and Nanoelectronics*, CRC Press, 2017, pp. 221–249.

[56] A. N. Whitehead and B. Russell, *Principia Mathematica*. University Press, 1910.

[57] J. Borghetti, G. S. Snider, P. J. Kuekes, J. J. Yang, D. R. Stewart, and R. S. Williams, “‘Memristive’ switches enable ‘stateful’ logic operations via material implication,” *Nature*, vol. 464, no. 7290, pp. 873–876, Apr. 2010, doi: 10.1038/nature08940.

[58] M. Endo, S. Kanai, S. Ikeda, F. Matsukura, and H. Ohno, “Electric-field effects on thickness dependent magnetic anisotropy of sputtered MgO/Co40Fe40B20/Ta structures,” *Appl. Phys. Lett.*, vol. 96, no. 21, 2010, doi: 10.1063/1.3429592.

[59] A. Jaiswal, A. Agrawal, and K. Roy, “In-situ, In-Memory Stateful Vector Logic Operations based on Voltage Controlled Magnetic Anisotropy,” *Sci. Rep.*, vol. 8, no. 1, p. 5738, Apr. 2018, doi: 10.1038/s41598-018-23886-2.

[60] S. Peng *et al.*, “Origin of interfacial perpendicular magnetic anisotropy in MgO/CoFe/metallic capping layer structures,” *Sci. Rep.*, vol. 5, no. 1, p. 18173, Dec. 2015, doi: 10.1038/srep18173.

[61] S. Ikeda *et al.*, “A perpendicular-anisotropy CoFeB–MgO magnetic tunnel junction,” *Nat. Mater.*, vol. 9, no. 9, pp. 721–724, Sep. 2010, doi: 10.1038/nmat2804.

[62] W. Kang *et al.*, “Yield and Reliability Improvement Techniques for Emerging Nonvolatile STT-MRAM,” *IEEE J. Emerg. Sel. Top. Circuits Syst.*, vol. 5, no. 1, pp. 28–39, Mar. 2015, doi: 10.1109/JETCAS.2014.2374291.

[63] N. Tezuka *et al.*, “Perpendicular Magnetic Tunnel Junctions With Low Resistance-Area Product: High Output Voltage and Bias Dependence of Magnetoresistance,” *IEEE Magn. Lett.*, vol. 7, pp. 1–4, 2016, doi: 10.1109/LMAG.2016.2584582.

[64] T. Nozaki *et al.*, “Recent Progress in the Voltage-Controlled Magnetic Anisotropy Effect and the Challenges Faced in Developing Voltage-Torque MRAM,” *Micromachines*, vol. 10, no. 5, p. 327, May 2019, doi: 10.3390/mi10050327.

[65] L. Wang *et al.*, “Voltage-Controlled Magnetic Tunnel Junctions for Processing-In-Memory Implementation,” *IEEE Electron Device Lett.*, vol. 39, no. 3, pp. 440–443, Mar. 2018, doi: 10.1109/LED.2018.2791510.

[66] E. Garzon *et al.*, “Exploiting Double-Barrier MTJs for Energy-Efficient Nanoscaled STT-MRAMs,” in *2019 16th International Conference on Synthesis, Modeling, Analysis and Simulation Methods and Applications to Circuit Design (SMACD)*, Jul. 2019, pp. 85–88, doi: 10.1109/SMACD.2019.8795223.

[67] A. A. Tulapurkar *et al.*, “Spin-torque diode effect in magnetic tunnel junctions,” *Nature*, vol. 438, no. 7066, pp. 339–342, Nov.

2005, doi: 10.1038/nature04207.

[68] C. Kittel, P. McEuen, and J. W. \& Sons, *Introduction to Solid State Physics*. John Wiley \& Sons, 2015.

[69] C. Wang, Y.-T. Cui, J. Z. Sun, J. A. Katine, R. A. Buhrman, and D. C. Ralph, "Sensitivity of spin-torque diodes for frequency-tunable resonant microwave detection," *J. Appl. Phys.*, vol. 106, no. 5, p. 053905, Sep. 2009, doi: 10.1063/1.3197137.

[70] O. Prokopenko, G. Melkov, E. Bankowski, T. Meitzler, V. Tiberkevich, and A. Slavin, "Noise properties of a resonance-type spin-torque microwave detector," *Appl. Phys. Lett.*, vol. 99, no. 3, p. 032507, Jul. 2011, doi: 10.1063/1.3612917.

[71] O. Golonzka *et al.*, "MRAM as Embedded Non-Volatile Memory Solution for 22FFL FinFET Technology," in *2018 IEEE International Electron Devices Meeting (IEDM)*, Dec. 2018, pp. 18.1.1-18.1.4, doi: 10.1109/IEDM.2018.8614620.

[72] G. Finocchio *et al.*, "Perspectives on spintronic diodes," *Appl. Phys. Lett.*, vol. 118, no. 16, p. 160502, Apr. 2021, doi: 10.1063/5.0048947.

[73] G. Finocchio *et al.*, "Skyrmion based microwave detectors and harvesting," *Appl. Phys. Lett.*, vol. 107, no. 26, p. 262401, 2015, doi: 10.1063/1.4938539.

[74] J. C. Sankey, Y.-T. Cui, J. Z. Sun, J. C. Slonczewski, R. A. Buhrman, and D. C. Ralph, "Measurement of the spin-transfer-torque vector in magnetic tunnel junctions," *Nat. Phys.*, vol. 4, no. 1, pp. 67–71, Jan. 2008, doi: 10.1038/nphys783.

[75] H. Kubota *et al.*, "Quantitative measurement of voltage dependence

of spin-transfer torque in MgO-based magnetic tunnel junctions," *Nat. Phys.*, vol. 4, no. 1, pp. 37–41, Jan. 2008, doi: 10.1038/nphys784.

[76] C. Wang, Y.-T. Cui, J. Z. Sun, J. A. Katine, R. A. Buhrman, and D. C. Ralph, "Bias and angular dependence of spin-transfer torque in magnetic tunnel junctions," *Phys. Rev. B*, vol. 79, no. 22, p. 224416, Jun. 2009, doi: 10.1103/PhysRevB.79.224416.

[77] B. Fang *et al.*, "Giant spin-torque diode sensitivity in the absence of bias magnetic field," *Nat. Commun.*, vol. 7, no. 1, p. 11259, Dec. 2016, doi: 10.1038/ncomms11259.

[78] B. Fang *et al.*, "Experimental Demonstration of Spintronic Broadband Microwave Detectors and Their Capability for Powering Nanodevices," *Phys. Rev. Appl.*, vol. 11, no. 1, p. 014022, Jan. 2019, doi: 10.1103/PhysRevApplied.11.014022.

[79] X. Cheng, J. A. Katine, G. E. Rowlands, and I. N. Krivorotov, "Nonlinear ferromagnetic resonance induced by spin torque in nanoscale magnetic tunnel junctions," *Appl. Phys. Lett.*, vol. 103, no. 8, p. 082402, Aug. 2013, doi: 10.1063/1.4819179.

[80] S. Miwa *et al.*, "Highly sensitive nanoscale spin-torque diode," *Nat. Mater.*, vol. 13, no. 1, pp. 50–56, Jan. 2014, doi: 10.1038/nmat3778.

[81] A. S. Jenkins *et al.*, "Spin-torque resonant expulsion of the vortex core for an efficient radiofrequency detection scheme," *Nat. Nanotechnol.*, vol. 11, no. 4, pp. 360–364, Apr. 2016, doi: 10.1038/nnano.2015.295.

[82] J. M. Algarín *et al.*, "High rectification sensitivity of

radiofrequency signal through adiabatic stochastic resonance in nanoscale magnetic tunnel junctions," *Appl. Phys. Lett.*, vol. 115, no. 19, p. 192402, Nov. 2019, doi: 10.1063/1.5123466.

[83] O. V. Prokopenko *et al.*, "Spin-torque microwave detector with out-of-plane precessing magnetic moment," *J. Appl. Phys.*, vol. 111, no. 12, p. 123904, Jun. 2012, doi: 10.1063/1.4729301.

[84] O. Prokopenko, G. Melkov, E. Bankowski, T. Meitzler, V. Tiberkevich, and A. Slavin, "Noise properties of a resonance-type spin-torque microwave detector," *Appl. Phys. Lett.*, vol. 99, no. 3, p. 032507, Jul. 2011, doi: 10.1063/1.3612917.

[85] L. Liu, T. Moriyama, D. C. Ralph, and R. A. Buhrman, "Spin-Torque Ferromagnetic Resonance Induced by the Spin Hall Effect," *Phys. Rev. Lett.*, vol. 106, no. 3, p. 036601, Jan. 2011, doi: 10.1103/PhysRevLett.106.036601.

[86] G. Siracusano *et al.*, "Intrinsic synchronization of an array of spin-torque oscillators driven by the spin-Hall effect," *J. Appl. Phys.*, vol. 117, no. 17, p. 17E504, 2015, doi: 10.1063/1.4914880.

[87] S. Lequeux *et al.*, "Increased magnetic damping of a single domain wall and adjacent magnetic domains detected by spin torque diode in a nanostripe," *Appl. Phys. Lett.*, vol. 107, no. 18, p. 182404, Nov. 2015, doi: 10.1063/1.4935203.

[88] D. Marković *et al.*, "Reservoir computing with the frequency, phase, and amplitude of spin-torque nano-oscillators," *Appl. Phys. Lett.*, vol. 114, no. 1, p. 012409, Jan. 2019, doi: 10.1063/1.5079305.

[89] J. Cai *et al.*, "Sparse neuromorphic computing based on spin-torque diodes," *Appl. Phys. Lett.*, vol. 114, no. 19, 2019, doi:

10.1063/1.5090566.

[90] L. Zhang *et al.*, “Ultrahigh detection sensitivity exceeding 105 V/W in spin-torque diode,” *Appl. Phys. Lett.*, vol. 113, no. 10, 2018, doi: 10.1063/1.5047547.

[91] C. Wang, Y. T. Cui, J. Z. Sun, J. A. Katine, R. A. Buhrman, and D. C. Ralph, “Sensitivity of spin-torque diodes for frequency-tunable resonant microwave detection,” *J. Appl. Phys.*, vol. 106, no. 5, pp. 1–6, 2009, doi: 10.1063/1.3197137.

[92] Y. S. Gui *et al.*, “High sensitivity microwave detection using a magnetic tunnel junction in the absence of an external applied magnetic field,” *Appl. Phys. Lett.*, vol. 106, no. 15, p. 152403, Apr. 2015, doi: 10.1063/1.4918677.

[93] W. Skowroński, M. Frankowski, J. Wrona, T. Stobiecki, P. Ogrodnik, and J. Barnaś, “Spin-torque diode radio-frequency detector with voltage tuned resonance,” *Appl. Phys. Lett.*, vol. 105, no. 7, p. 072409, Aug. 2014, doi: 10.1063/1.4893463.

[94] L. Fu *et al.*, “Microwave radar imaging using a solid state spintronic microwave sensor,” *Appl. Phys. Lett.*, vol. 105, no. 12, p. 122406, Sep. 2014, doi: 10.1063/1.4896691.

[95] L. Fu, Y. S. Gui, L. H. Bai, H. Guo, H. Abou-Rachid, and C.-M. Hu, “Microwave holography using a magnetic tunnel junction based spintronic microwave sensor,” *J. Appl. Phys.*, vol. 117, no. 21, p. 213902, Jun. 2015, doi: 10.1063/1.4921887.

[96] R. Tomasello *et al.*, “Antiferromagnetic Parametric Resonance Driven by Voltage-Controlled Magnetic Anisotropy,” *Phys. Rev. Appl.*, vol. 17, no. 3, p. 034004, Mar. 2022, doi:

10.1103/PhysRevApplied.17.034004.

[97] M. Díaz-Michelena, “Small magnetic sensors for space applications,” *Sensors*, vol. 9, no. 4, pp. 2271–2288, 2009, doi: 10.3390/s90402271.

[98] J. Bird and D. Arden, “Indoor navigation with foot-mounted strapdown inertial navigation and magnetic sensors [Emerging Opportunities for Localization and Tracking],” *Wirel. Commun. IEEE*, vol. 18(2), pp. 28–35, 2011, doi: 10.1109/MWC.2011.5751293.

[99] Z. Luo, Y. Xu, Y. Yang, and Y. Wu, “Magnetic angular position sensor enabled by spin-orbit torque,” *Appl. Phys. Lett.*, vol. 112, no. 26, p. 262405, 2018, doi: 10.1063/1.5038908.

[100] T. Reininger, F. Welker, and M. von Zeppelin, “Sensors in position control applications for industrial automation,” *Sensors Actuators A Phys.*, vol. 129, no. 1, pp. 270–274, 2006, doi: https://doi.org/10.1016/j.sna.2005.09.056.

[101] T. Uchiyama and J. Ma, “Development of pico tesla resolution amorphous wire magneto-impedance sensor for bio-magnetic field measurements,” *J. Magn. Magn. Mater.*, vol. 514, no. June, p. 167148, 2020, doi: 10.1016/j.jmmm.2020.167148.

[102] M. A. Khan, J. Sun, B. Li, A. Przybysz, and J. Kosel, “Magnetic sensors-A review and recent technologies,” *Eng. Res. Express*, vol. 3, no. 2, 2021, doi: 10.1088/2631-8695/ac0838.

[103] J. Fraden, *Handbook of Modern Sensors Fifth Edition*. 2016.

[104] S. M. S. O.W. Oluyombo, A. M. S. Tekanyi and B. Jimoh, “Improvement of Sensitivity and Noise of a Fluxgate

Magnetometer using Modified Firefly Optimization Algorithm," *Int. J. Eng. Res. Technol.*, vol. 4, no. 4, pp. 32–37, 2015, [Online]. Available: www.ijert.org.

[105] Z. Zeng *et al.*, "Ultralow-current-density and bias-field-free spin-transfer nano-oscillator," *Sci. Rep.*, vol. 3, no. 1, p. 1426, Dec. 2013, doi: 10.1038/srep01426.

[106] Z. Zeng, G. Finocchio, and H. Jiang, "Spin transfer nano-oscillators," *Nanoscale*, vol. 5, no. 6, p. 2219, 2013, doi: 10.1039/c2nr33407k.

[107] R. Tomasello, M. Carpentieri, and G. Finocchio, "Influence of the Dzyaloshinskii-Moriya interaction on the spin-torque diode effect," *J. Appl. Phys.*, vol. 115, no. 17, p. 17C730, 2014, doi: 10.1063/1.4867750.

[108] M. Löhndorf, T. Duenas, M. Tewes, E. Quandt, M. Rührig, and J. Wecker, "Highly sensitive strain sensors based on magnetic tunneling junctions," *Appl. Phys. Lett.*, vol. 81, no. 2, pp. 313–315, Jun. 2002, doi: 10.1063/1.1483123.

[109] S. Parkin, X. Jiang, C. Kaiser, A. Panchula, K. Roche, and M. Samant, "Magnetically engineered spintronic sensors and memory," *Proc. IEEE*, vol. 91, no. 5, pp. 661–680, 2003, doi: 10.1109/JPROC.2003.811807.

[110] G. Finocchio, I. N. Krivorotov, L. Torres, R. A. Buhrman, D. C. Ralph, and B. Azzerboni, "Magnetization reversal driven by spin-polarized current in exchange-biased nanoscale spin valves," *Phys. Rev. B*, vol. 76, no. 17, p. 174408, Nov. 2007, doi: 10.1103/PhysRevB.76.174408.

[111] G. Finocchio, B. Azzerboni, G. D. Fuchs, R. A. Buhrman, and L. Torres, “Micromagnetic modeling of magnetization switching driven by spin-polarized current in magnetic tunnel junctions,” *J. Appl. Phys.*, vol. 101, no. 6, p. 63914, 2007, doi: 10.1063/1.2496202.

[112] A. D. Kent and D. C. Worledge, “A new spin on magnetic memories,” *Nat. Nanotechnol.*, vol. 10, no. 3, pp. 187–191, 2015, doi: 10.1038/nnano.2015.24.

[113] S. Parkin and S.-H. Yang, “Memory on the racetrack,” *Nat. Nanotechnol.*, vol. 10, no. 3, pp. 195–198, 2015, doi: 10.1038/nnano.2015.41.

[114] V. Baltz, A. Manchon, M. Tsoi, T. Moriyama, T. Ono, and Y. Tserkovnyak, “Antiferromagnetic spintronics,” *Rev. Mod. Phys.*, vol. 90, no. 1, p. 15005, Feb. 2018, doi: 10.1103/RevModPhys.90.015005.

[115] E. Y. Vedmedenko *et al.*, “The 2020 magnetism roadmap,” *J. Phys. D. Appl. Phys.*, vol. 53, no. 45, p. 453001, 2020, doi: 10.1088/1361-6463/ab9d98.

[116] V. S. Pribiag, G. Finocchio, B. J. Williams, D. C. Ralph, and R. A. Buhrman, “Long-timescale fluctuations in zero-field magnetic vortex oscillations driven by dc spin-polarized current,” *Phys. Rev. B*, vol. 80, no. 18, p. 180411, Nov. 2009, doi: 10.1103/PhysRevB.80.180411.

[117] J. Torrejon *et al.*, “Neuromorphic computing with nanoscale spintronic oscillators,” *Nature*, vol. 547, no. 7664, pp. 428–431, Jul. 2017, doi: 10.1038/nature23011.

[118] M. Romera *et al.*, “Vowel recognition with four coupled spin-torque nano-oscillators,” *Nature*, vol. 563, no. 7730, pp. 230–234, Nov. 2018, doi: 10.1038/s41586-018-0632-y.

[119] S. Tsunegi *et al.*, “Physical reservoir computing based on spin torque oscillator with forced synchronization,” *Appl. Phys. Lett.*, vol. 114, no. 16, p. 164101, Apr. 2019, doi: 10.1063/1.5081797.

[120] T. Jungwirth, X. Marti, P. Wadley, and J. Wunderlich, “Antiferromagnetic spintronics.,” *Nat. Nanotechnol.*, vol. 11, no. 3, pp. 231–241, Mar. 2016, doi: 10.1038/nnano.2016.18.

[121] F. Büttner, I. Lemesh, and G. S. D. Beach, “Theory of isolated magnetic skyrmions: From fundamentals to room temperature applications,” *Sci. Rep.*, vol. 8, no. 1, p. 4464, 2018, doi: 10.1038/s41598-018-22242-8.

[122] S.-H. Yang, K.-S. Ryu, and S. Parkin, “Domain-wall velocities of up to 750 m s−1 driven by exchange-coupling torque in synthetic antiferromagnets,” *Nat. Nanotechnol.*, vol. 10, no. 3, pp. 221–226, 2015, doi: 10.1038/nnano.2014.324.

[123] K. Olejník *et al.*, “Terahertz electrical writing speed in an antiferromagnetic memory,” *Sci. Adv.*, vol. 4, no. 3, p. eaar3566, Mar. 2018, doi: 10.1126/sciadv.aar3566.

[124] A. S. Núñez, R. A. Duine, P. Haney, and A. H. MacDonald, “Theory of spin torques and giant magnetoresistance in antiferromagnetic metals,” *Phys. Rev. B*, vol. 73, no. 21, p. 214426, Jun. 2006, doi: 10.1103/PhysRevB.73.214426.

[125] T. Higo, D. Qu, Y. Li, C. L. Chien, Y. Otani, and S. Nakatsuji, “Anomalous Hall effect in thin films of the Weyl antiferromagnet

Mn3Sn," *Appl. Phys. Lett.*, vol. 113, no. 20, p. 202402, Nov. 2018, doi: 10.1063/1.5064697.

[126] T. Moriyama, K. Oda, T. Ohkochi, M. Kimata, and T. Ono, "Spin torque control of antiferromagnetic moments in NiO," *Sci. Rep.*, vol. 8, no. 1, p. 14167, 2018, doi: 10.1038/s41598-018-32508-w.

[127] J. Godinho *et al.*, "Electrically induced and detected Néel vector reversal in a collinear antiferromagnet," *Nat. Commun.*, vol. 9, no. 1, p. 4686, 2018, doi: 10.1038/s41467-018-07092-2.

[128] C. Wang, H. Seinige, G. Cao, J.-S. Zhou, J. B. Goodenough, and M. Tsoi, "Anisotropic Magnetoresistance in Antiferromagnetic ${\mathrm{Sr}}_{2}{\mathrm{IrO}}_{4}$," *Phys. Rev. X*, vol. 4, no. 4, p. 41034, Nov. 2014, doi: 10.1103/PhysRevX.4.041034.

[129] R. F. L. Evans, T. A. Ostler, R. W. Chantrell, I. Radu, and T. Rasing, "Ultrafast thermally induced magnetic switching in synthetic ferrimagnets," *Appl. Phys. Lett.*, vol. 104, no. 8, p. 82410, Feb. 2014, doi: 10.1063/1.4867015.

[130] J. Finley and L. Liu, "Spintronics with compensated ferrimagnets," *Appl. Phys. Lett.*, vol. 116, no. 11, p. 110501, Mar. 2020, doi: 10.1063/1.5144076.

[131] K. Fleischer *et al.*, "Magneto-optic Kerr effect in a spin-polarized zero-moment ferrimagnet," *Phys. Rev. B*, vol. 98, no. 13, p. 134445, Oct. 2018, doi: 10.1103/PhysRevB.98.134445.

[132] A. Hrabec, S. Skskdjc, S. Pizzini, and L. Ranno, "Magnetization reversal in composition-controlled Gd1-xCox ferrimagnetic films close to compensation composition," *Appl. Phys. Lett. - APPL PHYS LETT*, vol. 99, Aug. 2011, doi: 10.1063/1.3609860.

[133] K. Ueda, M. Mann, C.-F. Pai, A.-J. Tan, and G. S. D. Beach, "Spin-orbit torques in Ta/TbxCo100-x ferrimagnetic alloy films with bulk perpendicular magnetic anisotropy," *Appl. Phys. Lett.*, vol. 109, no. 23, p. 232403, Dec. 2016, doi: 10.1063/1.4971393.

[134] Y. Mimura, N. Imamura, and Y. Kushiro, "Hall effect in rare-earth–transition-metal amorphous alloy films," *J. Appl. Phys.*, vol. 47, no. 7, pp. 3371–3373, Jul. 1976, doi: 10.1063/1.323098.

[135] N. Roschewsky *et al.*, "Spin-orbit torques in ferrimagnetic GdFeCo alloys," *Appl. Phys. Lett.*, vol. 109, no. 11, p. 112403, Sep. 2016, doi: 10.1063/1.4962812.

[136] J. Han *et al.*, "Scaling of the anomalous Hall effect in ferrimagnetic Co90Gd10 thin films," *IEEE Trans. Magn.*, vol. 51, p. 1, Nov. 2015, doi: 10.1109/TMAG.2015.2443112.

[137] S. Woo *et al.*, "Current-driven dynamics and inhibition of the skyrmion Hall effect of ferrimagnetic skyrmions in GdFeCo films," *Nat. Commun.*, vol. 9, no. 1, p. 959, Dec. 2018, doi: 10.1038/s41467-018-03378-7.

[138] L. Caretta *et al.*, "Fast current-driven domain walls and small skyrmions in a compensated ferrimagnet," *Nat. Nanotechnol.*, vol. 13, no. 12, pp. 1154–1160, 2018, doi: 10.1038/s41565-018-0255-3.

[139] Y. Hirata *et al.*, "Correlation between compensation temperatures of magnetization and angular momentum in GdFeCo ferrimagnets," *Phys. Rev. B*, vol. 97, no. 22, p. 220403, Jun. 2018, doi: 10.1103/PhysRevB.97.220403.

[140] I. Radu *et al.*, "Transient ferromagnetic-like state mediating ultrafast reversal of antiferromagnetically coupled spins," *Nature*,

vol. 472, no. 7342, pp. 205–208, 2011, doi: 10.1038/nature09901.

[141] M. S. El Hadri *et al.*, “Two types of all-optical magnetization switching mechanisms using femtosecond laser pulses,” *Phys. Rev. B*, vol. 94, no. 6, p. 64412, 2016, doi: 10.1103/PhysRevB.94.064412.

[142] M. L. M. Lalieu, R. Lavrijsen, and B. Koopmans, “Integrating all-optical switching with spintronics,” *Nat. Commun.*, vol. 10, no. 1, p. 110, 2019, doi: 10.1038/s41467-018-08062-4.

[143] S.-G. Je *et al.*, “Spin-orbit torque-induced switching in ferrimagnetic alloys: Experiments and modeling,” *Appl. Phys. Lett.*, vol. 112, no. 6, p. 62401, 2018, doi: 10.1063/1.5017738.

[144] I. Lisenkov, R. Khymyn, J. Åkerman, N. X. Sun, and B. A. Ivanov, “Subterahertz ferrimagnetic spin-transfer torque oscillator,” *Phys. Rev. B*, vol. 100, no. 10, p. 100409, Sep. 2019, doi: 10.1103/PhysRevB.100.100409.

[145] V. E. Demidov *et al.*, “Magnetic nano-oscillator driven by pure spin current,” *Nat. Mater.*, vol. 11, no. 12, pp. 1028–1031, 2012, doi: 10.1038/nmat3459.

[146] J. E. Hirsch, “Spin Hall Effect,” *Phys. Rev. Lett.*, vol. 83, no. 9, pp. 1834–1837, Aug. 1999, doi: 10.1103/PhysRevLett.83.1834.

[147] L. Liu, T. Moriyama, D. C. Ralph, and R. A. Buhrman, “Spin-Torque Ferromagnetic Resonance Induced by the Spin Hall Effect,” *Phys. Rev. Lett.*, vol. 106, no. 3, p. 36601, Jan. 2011, doi: 10.1103/PhysRevLett.106.036601.

[148] Y. A. Bychkov and E. I. Rashba, “Oscillatory effects and the magnetic susceptibility of carriers in inversion layers,” *J. Phys. C*

Solid State Phys., vol. 17, no. 33, p. 6039, 1984, doi: 10.1088/0022-3719/17/33/015.

[149] A. Manchon and S. Zhang, "Theory of nonequilibrium intrinsic spin torque in a single nanomagnet," *Phys. Rev. B*, vol. 78, no. 21, p. 212405, 2008, doi: 10.1103/PhysRevB.78.212405.

[150] S. Tacchi *et al.*, "Interfacial Dzyaloshinskii-Moriya Interaction in <math display="inline"> <mrow> <mi>Pt</mi> <mo>/</mo> <mi>CoFeB</mi> </mrow> </math> Films: Effect of the Heavy-Metal Thickness," *Phys. Rev. Lett.*, vol. 118, no. 14, p. 147201, Apr. 2017, doi: 10.1103/PhysRevLett.118.147201.

[151] K.-J. Kim *et al.*, "Fast domain wall motion in the vicinity of the angular momentum compensation temperature of ferrimagnets.," *Nat. Mater.*, vol. 16, no. 12, pp. 1187–1192, Dec. 2017, doi: 10.1038/nmat4990.

[152] R. Bläsing *et al.*, "Exchange coupling torque in ferrimagnetic Co/Gd bilayer maximized near angular momentum compensation temperature," *Nat. Commun.*, vol. 9, no. 1, p. 4984, 2018, doi: 10.1038/s41467-018-07373-w.

[153] Z. Zhu, X. Fong, and G. Liang, "Damping-like spin-orbit-torque-induced magnetization dynamics in ferrimagnets based on Landau-Lifshitz-Bloch equation," *J. Appl. Phys.*, vol. 124, no. 19, p. 193901, 2018, doi: 10.1063/1.5048040.

[154] K. Cai *et al.*, "Ultrafast and energy-efficient spin–orbit torque switching in compensated ferrimagnets," *Nat. Electron.*, vol. 3, no. 1, pp. 37–42, 2020, doi: 10.1038/s41928-019-0345-8.

[155] S. K. Kim, "Fast and efficient switching with ferrimagnets," *Nat.*

Electron., vol. 3, no. 1, pp. 18–19, 2020, doi: 10.1038/s41928-019-0352-9.

[156] R. Khymyn, I. Lisenkov, V. Tiberkevich, B. A. Ivanov, and A. Slavin, "Antiferromagnetic THz-frequency Josephson-like Oscillator Driven by Spin Current," *Sci. Rep.*, vol. 7, no. 1, p. 43705, May 2017, doi: 10.1038/srep43705.

[157] V. Puliafito *et al.*, "Micromagnetic modeling of terahertz oscillations in an antiferromagnetic material driven by the spin Hall effect," *Phys. Rev. B*, vol. 99, no. 2, p. 24405, Jan. 2019, doi: 10.1103/PhysRevB.99.024405.

[158] M. Binder *et al.*, "Magnetization dynamics of the ferrimagnet CoGd near the compensation of magnetization and angular momentum," *Phys. Rev. B*, vol. 74, no. 13, p. 134404, Oct. 2006, doi: 10.1103/PhysRevB.74.134404.

[159] R. Tomasello *et al.*, "Performance of synthetic antiferromagnetic racetrack memory: domain wall versus skyrmion," *J. Phys. D. Appl. Phys.*, vol. 50, no. 32, p. 325302, 2017, doi: 10.1088/1361-6463/aa7a98.

[160] M. Ding and S. J. Poon, "Tunable perpendicular magnetic anisotropy in GdFeCo amorphous films," *J. Magn. Magn. Mater.*, vol. 339, pp. 51–55, 2013, doi: https://doi.org/10.1016/j.jmmm.2013.03.007.